Applied Energy 360 (2024) 122746

Contents lists available at ScienceDirect

Applied Energy

journal homepage: www.elsevier.com/locate/apenergy

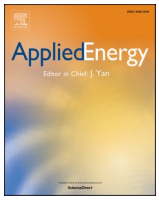

A new multiphysics modeling framework to simulate coupled electrochemical-thermal-electrical phenomena in Li-ion battery packs

S.M. Jordan [a], C.O. Schreiber [a], M. Parhizi [b], K. Shah [a,*]

[a] Department of Mechanical Engineering, The University of Alabama, Box 870276, Tuscaloosa, AL 35487-0276, USA
[b] Electrochemical Safety Research Institute, UL Research Institutes, 5000 Gulf Fwy, UHTB, Bldg 5, Rm 138, Houston, TX 77204

HIGHLIGHTS

- Developed a multiphysics modeling framework to simulate electrochemical-thermal characteristics of Li-ion battery packs
- Flexible, scalable, and efficient physics-based simulation of Li-ion battery packs
- In-depth analysis of Li-ion battery pack at various operating conditions, including extreme thermal conditions
- Effect of cell-to-cell manufacturing variation on cell-level and pack-level electrochemical and thermal characteristics

ARTICLE INFO

Keywords:
Lithium-ion batteries
Electrochemical engineering
Battery thermal management
Physics-based battery models
Battery pack modeling
Battery pack aging
Cell balancing

ABSTRACT

This study introduces a streamlined modeling framework that integrates a volume-averaged thermal (VAT) model with the Tank-in-Series battery model, a recently developed volume-averaged electrochemical model. The framework enables efficient simulations of electrochemical-thermal interactions in large-scale battery packs. This framework is used to investigate the effects of coolant flow rates and inlet temperature, initial and ambient temperatures, battery pack configurations, and cell-to-cell manufacturing related variations. Results showed a notable current distribution variation among modules connected in parallel at the end of discharge and beginning of charge. This is found to be directly related to the temperature variation in the battery pack governed by the coolant mass flow rate. Additionally, with the introduction of a 0.5% cell-to-cell to variation in the cell design parameters for the purpose of simulating manufacturing variation, a significant voltage variation of over 0.2 V across cells is found to be possible. Furthermore, rapidly changing the inlet temperatures to simulate a potential battery management system failure indicated the risk of some cells in the pack exceeding the desired cut-off voltage. The present framework can be used to design battery packs with effective thermal management strategies, enhancing the overall reliability and performance of battery systems.

1. Introduction

Due to the advances in the manufacturing of Li-ion batteries in the past decade, combined with scientific advances in the technology over the last three decades resulting in improved performance, life, and safety, Li-ion batteries are currently being used in a wide variety of applications. As popular as they already are, Li-ion batteries continue to see increasing demand in consumer electronics, electric transportation, and large-scale energy storage fields. For reference, the Department of Energy is projecting that the demand for ground-based electric vehicle energy storage will triple in the coming decade [1]. However, to further expand the use of batteries in the transportation and energy sectors and improve their performance, longevity, and safety, the design and operation-related challenges spanning from cell- to pack-level must be addressed. These challenges are extremely nuanced and intrinsically linked to each other; they include issues such as suboptimal performance at extreme temperatures exacerbated by thermal imbalance at the pack-level [2–9], cell balancing issues [10–19], uneven aging [20–22], cell-to-cell performance variation [23–26], and safety [27–30].

Thermal imbalance in a battery pack is primarily due to inadequate thermal management, leading to significant temperature variation across cells. At low temperatures, cells become highly prone to degradation due to lithium plating, specifically during charging [2–4]. Additionally, battery efficiency also reduces at low temperatures due to

* Corresponding author at: 3043 H.M. Comer, 245 7th Avenue, Tuscaloosa, AL 35401, USA.
E-mail address: krishna.shah@ua.edu (K. Shah).

https://doi.org/10.1016/j.apenergy.2024.122746
Received 4 September 2023; Received in revised form 6 January 2024; Accepted 21 January 2024
Available online 20 February 2024

sluggish electrolyte transport and slower reaction kinetics, increasing overall cell resistance [3]. Zilberman et al. showed that even a temperature gradient of 5 °C within a module can lead to drastic differences in capacities between cells when cycled [5]. At high temperatures, cells become prone to degradation from side reactions such as solid electrolyte interphase (SEI) growth [6,7]. Temperature variation within a module/pack at high temperatures can lead to uneven degradation of cells in a battery pack. For example, in Chiu et al., a temperature gradient of 18 °C at an average temperature of 60 °C was found to have a 7% greater capacity fade versus a negligible temperature gradient at 60 °C [8]. In addition to uneven degradation, Feng et al. found that a 5 °C gradient could induce a pack-level capacity loss of 1.5% to 2% over one cycle [9]. In addition to cell degradation, thermal imbalance within a battery pack may also lead to charge imbalance [11–14]. Rahn et al. showed that a 5 °C difference between two parallel cells could result in a current difference of up to 40% [14].

Charge imbalance between the cells of a battery pack can result in major problems caused by cell voltages exceeding recommended manufacturer limits, leading to overcharge and overdischarge scenarios. Charge imbalance is not only induced by temperature variation, but can also be caused by variations between cells' performances due to manufacturing variation, among other things [15]. This can lead to uneven current distributions, as seen in the research by Liu et al. In their work, Liu et al. performed experiments on a 6P1S battery module, where they found that upon initial discharge, there was a high level of current variation between cells, leading to complex current distributions and an increase in localized heating of cells furthest from the load point [24]. Additionally, pack construction, in particular cell interconnects, can cause charge imbalance issues in a battery pack [16]. Regardless of the cause, the charge imbalance can increase the likelihood of overcharge and overdischarge at the cell level, which can result in electrical abuse and lead to severe cell degradation and significant safety concerns [17–19].

The uneven degradation caused by thermal imbalance and charge imbalance within the battery pack ultimately leads to uneven aging between cells of the battery pack [20]. Uneven aging is a critical problem, leading to uneven heat generation and state-of-charge (SOC) imbalance within a pack, further exacerbating degradation [21]. This forms a positive feedback loop where the battery pack is degraded at an accelerated rate because of cells growing further apart in terms of SOC and state of health (SOH). The problem of uneven aging is made worse when considering the impact of manufacturing cell-to-cell variation [22]. In Baumhöfer et al., a 21% capacity variation arose between 48 commercial cells of the same type that were cycled 1200 times in homogeneous conditions [25]. In Preger et al., a comparison between the results of different battery cycling studies was performed, and it was found that even among the cells of the same type cycled at the same operating conditions and rates, there were significant differences in the capacity fade trends [26]. Due to uneven degradation and manufacturing variations present in cells, proper consideration of uneven aging is crucial when modeling and designing battery packs for consumer use. Ultimately, the aim of understanding battery degradation and safety, along with their fundamental mechanisms, is to increase battery longevity and efficiency. This also serves to avert disastrous thermal runaway events that can cause temperatures to soar as high as 900 °C, giving rise to exceedingly perilous and life-threatening situations [31].

While there have been many advances in studying these issues, both through experimental testing and multiscale physics-based simulations, understanding of these issues remains largely qualitative, especially at the pack-level. Although experimental testing provides the most reliable approach for studying many of these issues, it is time- and cost-intensive, particularly for experiments involving large battery packs under a wide variety of operating conditions. Additionally, without postmortem analysis, experimental testing alone cannot provide fundamental insights into these issues [32,33]. Even though performing postmortem and/or in-operando characterization on a small number of battery cells can help identify underlying mechanisms dictating performance, degradation, and safety issues, this is not a viable strategy to study a battery pack which contains hundreds, if not thousands, of battery cells. Therefore, combining modeling and simulation at the pack-level with experimental testing at the cell level, including postmortem/in-operando characterization, can provide a practical pathway to gain insights into these issues spanning multiple length scales and develop effective engineering solutions.

Presently, simplified equivalent circuit and empirical models are typically used to simulate battery packs [34,35]. Since these models do not capture various physical phenomena and electrochemical processes taking place inside the battery, they cannot provide necessary insights into the aforementioned pack-level issues. In addition to equivalent circuit models, there are many modeling and simulation studies on thermal management of battery packs. However, many of these studies are limited to studying heat transfer and fluid flow without capturing the effects of temperature on the life and performance of batteries [36–41]. For example, in the case of Z. Liu et al. [37], the battery cells were simplified to be resistors for the purpose of simulation. In J. Tete et al. [41], batteries were considered constant heat source terms. While such simplifications in these studies provide relatively straightforward means to design and analyze battery thermal management systems (BTMS), the effectiveness of these thermal management systems in prolonging battery life and enhancing performance is not well understood or demonstrated. This is primarily due to the simplifications made to the complicated physics and electrochemical reactions within the battery while developing such models.

At the scale of a single Li-ion cell, many physics-based models have been developed incorporating various processes, including transport processes, reaction kinetics, thermal effect, and degradation mechanisms [42–52]. Some notable works include the pseudo-two-dimensional (P2D) model by M. Doyle et al. [42] and the single-particle model (SPM) by M. Guo et al. [43]. Studies focused on modeling the degradation at the cell level include works focused on modeling SEI growth [46], lithium plating [47], particle cracking [48], temperature-dependent degradation methods [49], and combinations of the aforementioned processes [50,51]. However, all these modeling studies are at the single-cell level. One of the first noteworthy works on pack-level modeling by M. Guo et al. involved using a thermal SPM; however, this study considered a simplified natural convection boundary condition and an electrochemical model that ignores lithium-ion transport in the electrolyte – limiting its applicability to low-rate applications [53]. Another research attempt by Smith et al. used a one-dimensional electrochemical model to simulate a 72-cell battery pack but assumed state-of-charge and temperature to be uniform throughout the battery pack [54]. Such simplifications fail to accurately capture various heat transfer, electrochemical, and electrical processes in a typical battery pack with a thermal management system. Other similar studies have also been subject to similar limitations [55–57]. Since many BTMS involve heat transfer processes significantly more complex than the simplified pack-level thermal models in these past studies can capture, a more rigorous modeling approach is necessary to enable accurate prediction of the temperature of battery cells in a battery pack and the resulting effect on electrochemical performance of individual battery cells in the pack.

A robust physics-based electrochemical model at the battery cell level applied to simulate each battery cell in the pack coupled with a thermal model for battery cells and thermal management system can help improve the fundamental understanding of pack-level performance, aging, and safety characteristics. Recent studies have incorporated battery thermal management simulations coupled with cell-level electrochemical simulations [57–64]. In Bahiraei et al., a 1D-electrochemical-thermal model coupled with a BTMS computational fluid dynamics (CFD) simulation was created but only used to analyze a six-cell module [59]. In Liang et al., a 1D-multilayered-electrochemical-thermal

model coupled with a BTMS thermal model was used to study temperature imbalance effects on a battery module. However, the coolant temperature used to model the convective heat transfer was an average value, and the convective heat transfer coefficients were chosen to induce uneven temperature [60]. In Wang et al., a 1D-electrochemical-thermal model coupled with CFD BTMS simulations was used to analyze a liquid-cooled battery pack [61]. However, this study only used 24 prismatic cells and focused primarily on the temperature gradient within the pack. In Pordanjani et al., a P2D model coupled with CFD BTMS simulations was used to analyze the temperature gradients and flow fields of multiple air-cooled battery pack configurations, but these packs were limited to 36 cylindrical cells, and there was no discussion pertaining to the electrochemical behavior of the modeled cells [63]. In Z. Guo et al. and Zadeh et al., electrochemical models were coupled with CFD models and used to investigate cell degradation under different thermal management systems [62,64]. While these studies provide valuable insights into the roles of BTMS heat pipe formation and the use of phase change materials, the studies are limited by the number of cells used for investigation.

While the aforementioned studies contribute to greater understanding of the complex interactions between multiple connected cells, they often require some simplifications and are limited to relatively small battery modules/packs compared to a typical battery pack, consisting of hundreds to thousands of cells, that would be used in applications such as electric vehicles, grid energy storage, and aerospace applications. Additionally, many of these studies primarily focus on the temperature and temperature variation within the battery pack and not the effect of temperature and cell-to-cell variation on battery pack performance characteristics, such as cell and pack voltage and current distribution within a battery pack/module. Finally, none of the past studies mentioned above provide a flexible, scalable, and computationally efficient modeling approach to study battery systems of various sizes, configurations, and complexity in design. This type of modeling capability would be of significant value to the research community for designing and analyzing battery systems for maximizing performance, minimizing aging, and enhancing safety.

The present work addresses the aforementioned limitations in pack-level modeling by introducing a versatile, scalable, and computationally efficient framework. This framework is designed to analyze large-format battery packs comprising hundreds to thousands of cells. The proposed framework can simulate many different types of BTMS with ease, due to the volume-averaging process used in this work. The framework not only calculates the cell temperature and temperature variations among cells in the pack, but also simulates how temperature affects the electrochemical performance of individual cells. Additionally, the framework can model effect of cell-to-cell manufacturing variation and initial charge imbalance in the battery pack on the electrochemical and thermal behavior of the cells and pack level performance. Although not included in the present work, various cell degradation mechanisms can be incorporated in the framework in a straightforward manner, allowing researchers to study how thermal imbalance, charge imbalance, and manufacturer variance impact and drive uneven degradation within large-format battery packs. This framework will provide researchers with a flexible tool to model various emerging pack designs, capable of studying how different thermal management systems and pack designs impact the electrochemical performance of each individual cell within the pack and the overall pack performance.

In this paper, a flexible, scalable, and computationally efficient modeling framework using a volume-averaged thermal (VAT) model consisting of volume-averaged energy equations for battery cells and coolant coupled with a volume-averaged Tank-in-series electrochemical battery model reported in the literature is developed and utilized to simulate large battery packs under a wide range of scenarios. The rest of the paper is organized as follows: Section 2.1 describes the mathematical formulation for the VAT model used to solve for battery cell and coolant temperature. Section 2.2 provides all the equations and constitutive relationships for the electrochemical cell model known as the Tank-in-Series model [65]. Section 2.3 describes the electrical model used to capture the pack configurations considered in this study, including the equations used to model series and parallel connections. Section 2.4 presents the coupling of these three models, forming the overall framework. In Section 3, we perform a detailed analysis on battery packs under different operating conditions, considering effects of cell-to-cell variations due to possible manufacturing discrepancies, and considering effects of extreme and rapidly changing temperatures, including studying the electrochemical and thermal behavior of individual batteries in the pack. We also provide validation of the VAT modeling approach by applying it to two different pack designs, one involving prismatic/pouch cells and the other involving cylindrical cells similar to the Tesla Model S EV battery pack [66], and comparing the temperature calculated from the VAT models with full-order CFD models. This section also includes a discussion on the limitation of the modeling framework and the potential future work building on this modeling framework and the findings presented in this study. Section 4 summarizes the key contributions of this work, significant findings from the simulation studies, and possible future work expanding on this research.

2. Mathematical framework

This section describes the mathematical framework consisting of a volume-averaged thermal model, a volume-averaged Tank-in-Series electrochemical model, and a 0D electrical model. Each of these models will be discussed in detail next.

2.1. Volume-averaged thermal model

This subsection presents the mathematical formulation of the volume-averaged thermal model. Details on the methodology and definitions used in deriving the volume-averaged energy conversation equations are provided by Whitaker et al. and others [67,68]. Definitions for nomenclature used in the following section can be found in Table 1 below.

The general governing equations used to describe the laminar thermal energy transport in the coolant of the BTMS and the thermal diffusion in the battery cell are as given below,

$$\rho_f c_{p,f} \frac{\partial T_f}{\partial t} + \rho_f c_{p,f} \nabla \bullet Tu = \nabla \bullet \left(k_f \nabla T\right) \tag{1}$$

$$\rho_s C_{p,s} \frac{\partial T_s}{\partial t} = \nabla \bullet \left(k_s \nabla T\right) + q^{'''} \tag{2}$$

Table 1
Nomenclature used in *Thermal Model* section for mathematical equations.

Nomenclature for *Thermal Model*	
ρ_f	Fluid density, **kg/m^3**
$c_{p,f}$	Specific heat of fluid, **J/(kg K)**
$\bar{T}_f$	Intrinsic average fluid temperature, **K**
$\bar{T}_s$	Intrinsic average solid temperature, **K**
$\bar{u}$	Average fluid velocity, **m/s**
u,v	x, y component of fluid velocity, **m/s**
k	Thermal conductivity, **W/(m K)**
$\langle m \rangle$	Average porosity
$S_{f,1}$	Specific solid-fluid interface area, **m^2/m^3**
$S_{f,2}$	Specific solid surface area without active cooling/heating, **m^2/m^3**
h	Convective heat transfer coefficient, **W/(m^2 K)**
ρ_s	Solid density, **kg/m^3**
$C_{p,s}$	Specific heat of solid, **J/(kg K)**
m_s	Mass of solid, **kg**
Q	Heat generation, **W**
$q^{'''}$	Volumetric heat generation, **W/m^3**
t	Time, **s**
x,y	Spatial coordinate, **m**

Where $q^{'''}$ is the volumetric heat generation rate of the battery cell. The subscripts s and f are used to indicate solid and fluid domains which refers to battery cells and coolant domains, respectively.

Although only the governing equations for energy conservation are given in Eqs. (1) and (3) prior to volume-averaging, appropriate boundary conditions are required at the interfaces and other boundaries, where applicable. At the interface, flux conservation and temperature continuity boundary conditions are applied. The boundary conditions at the other boundaries will depend on the system design and the assumptions made.

It should be noted that the coolant flow and heat transfer in the coolant and the battery cell are expressed in the general vector form in the above equations. By applying the procedure of volume-averaging theory outlined in Whitaker et al., Eqs. (1) and (2) are transformed into the following volume-averaged equations,

$$\langle m\rangle\rho_f c_{p,f}\frac{\partial \bar{T}_f}{\partial t}+\rho_f c_{p,f}\langle m\rangle\bar{u}\nabla\bar{T}_f = +hS_{f,1}\left(\bar{T}_s-\bar{T}_f\right) \tag{3}$$

$$(1-\langle m\rangle)\rho_s C_{p,s}\frac{\partial \bar{T}_s}{\partial t}=\nabla\bullet\left((1-\langle m\rangle)k_s\nabla\bar{T}_s\right)+(1-\langle m\rangle)q^{'''}-hS_{f,1}\left(\bar{T}_s-\bar{T}_f\right)-US_{f,2}(\bar{T}_s-T_\infty) \tag{4}$$

When Eqs. (1) and (2) are volume-averaged, the thermal energy conservation at the interface applied through the interfacial flux boundary condition in the full-order model appears as a source term representing convective heat transfer at the battery cell surface due to the flow of the coolant. The convective heat transfer coefficient (h) is calculated by evaluating the closure term resulting from the integration by parts performed on the conduction term in both Eqs. (1) and (2) while volume averaging. The equation to calculate h based on the evaluation of the closure term is given in the supplementary document. More details on the derivation of the volume-averaged equations and closure term evaluation can be found in past studies [67,68]. The additional source terms in Eq. (4) account for heat transfer between the battery cell and the battery cell/pack surrounding through the faces of the cell that are not actively cooled/heated by the thermal management system. The overall heat transfer coefficient (U) in this term may include various thermal resistances from these faces of the cell to the outer surface of the pack and convective heat transfer resistance from the outer surface to the surrounding air.

The closure terms are evaluated using full-order steady-state CFD simulations, which leads to the determination of an average convective heat transfer coefficient on the cooled surface of each cell. The full-order, steady-state CFD simulations solve continuity, momentum, and energy equations on a sufficiently refined mesh to compute accurate velocity and temperature fields capturing the velocity and thermal boundary layers in the fluid domain. The effect of the velocity and fluid phase temperature fields, specifically velocity and thermal boundary layers, on the interfacial heat transfer is captured via the h calculated from the full-order CFD simulations. For heat transfer through the rest of the surface of the cell, the overall heat transfer coefficient, U, can be determined by representing the heat transfer pathways from the cell to the surroundings as a thermal circuit or by using full-order CFD simulation to solve closure problems pertaining to the applicable faces of the cell. This will be done in the same way as determining h in the present work. For simplicity, U is considered to be 10 W/m^{2}K in this study which is representative of natural convection.

In the present work, cell-centered finite volume method is used to discretize the volume-averaged equations. Using these volume-averaged equations drastically reduces the number of discretized equations needed to be solved to accurately calculate battery cell temperature. Instead of each battery and accompanying coolant channel section requiring refined mesh leading to a large number of finite volumes and discretized equations, only one control volume is used to represent each such section, resulting in only two volume-averaged heat equations, one for the coolant and the other for the battery cell. This is particularly beneficial when modeling and simulating large battery packs. This method drastically reduces computational time while maintaining accuracy, as discussed in the next section. By reducing the computational requirements for modeling heat transfer processes, fully coupled simulation of electrochemical phenomena inside each cell within the battery pack and pack-level heat transfer phenomena is made practically possible, particularly for large battery packs. The volume-averaged electrochemical model to be coupled with this volume-average thermal model will be discussed next.

2.2. Volume-averaged Tank-in-Series electrochemical model

The electrochemical model used in this work is the Tank-in-Series model detailed in Subramaniam et al. [45,69]. The model has been derived by volume averaging the well-known P2D model over the cathode-anode-separator regions, allowing for quicker and

Table 2
Nomenclature used in *Electrochemical Model* mathematical equations.

Nomenclature for *Electrochemical Model*			
$\alpha_{a,1}$	Anodic activation coefficient, +ve	ε_1	Porosity, +ve
$\alpha_{c,1}$	Cathodic activation coefficient, +ve	ε_2	Porosity, sep
$\alpha_{a,3}$	Anodic activation coefficient, −ve	ε_3	Porosity, −ve
$\alpha_{c,3}$	Cathodic activation coefficient, −ve	k_1	Reaction rate constant, +ve
D	Liquid phase diffusion coefficient	k_3	Reaction rate constant, −ve
r_1	Electrode particle radius, +ve	l_1	Electrode thickness, +ve
r_3	Electrode particle radius, −ve	l_3	Electrode thickness, −ve
$D_{s,1}$	Solid phase diffusivity, +ve	l_2	Separator thickness
$D_{s,2}$	Solid phase diffusivity, −ve	t_i	Transference number
b_1	Bruggeman coefficient, +ve	$\phi_{l,1}$	Electrolyte potential, +ve
b_2	Bruggeman coefficient, sep	$\phi_{l,3}$	Electrolyte potential, −ve
b_3	Bruggeman coefficient, −ve	$c_3^{s,max}$	Maximum solid phase concentration, −ve
$\phi_{l,2}$	Electrolyte potential in separator	$c_1^{s,surf}$	Surface solid phase concentration, −ve
$c_1^{s,max}$	Maximum solid phase concentration, +ve	T_{ref}	Reference temperature, 298.15 K
$c_1^{s,surf}$	Surface solid phase concentration, +ve	κ	Ionic conductivity
f_p	Filler fraction, +ve	η_3	Activation overpotential, −ve
f_n	Filler fraction, −ve	c_2	Electrolyte lithium concentration, separator
η_1	Activation overpotential, +ve	c_{12}	Electrolyte lithium concentration, +ve interface
c_1	Electrolyte lithium concentration, +ve	a_1	Specific area of cathode active material
c_3	Electrolyte lithium concentration, −ve	T	Temperature
c_{23}	Electrolyte lithium concentration, −ve interface	j_3	Anode molar flux
a_3	Specific area of anode active material	F	Faraday's Constant
j_1	Cathode molar flux	R	Gas constant
i_{app}	Applied current density	A_{cc}	Current collector area

computationally efficient calculations. The governing equations to be solved in each region are detailed below. The set of equations might be slightly different from Subramaniam et al. due to the need to change the reference potential location to make the model suitable for pack level modeling. The variables and parameters in these equations can be found in Table 2.

2.2.1. Cathode equations

The following equations are used to model the physical and electrochemical processes within the cathode of the cell.

$$\frac{dc_1}{dt} = \frac{\frac{2(D(c_{12},T))(c_2-c_1)}{\frac{l_1}{\varepsilon_1^{b_1}}+\frac{l_2}{\varepsilon_2^{b_2}}}}{\varepsilon_1 l_1} + a_i(1-t_i)\frac{j_1}{\varepsilon_1} \tag{5}$$

Eq. (5) is the volume-averaged mass balance equation for the lithium ions in the electrolyte in the cathode.

$$i_{app} = -2\kappa\left(c_{12},T\right)\frac{\left(\phi_{l,2}-\phi_{l,1}\right)}{\left(\frac{l_1}{\varepsilon_1^{b_1}}+\frac{l_2}{\varepsilon_2^{b_2}}\right)} + \frac{4RT(1-t_i)}{F}\frac{\kappa(c_{12},T)(c_2-c_1)}{\left(\frac{l_1}{\varepsilon_1^{b_1}}+\frac{l_2}{\varepsilon_2^{b_2}}\right)c_{12}} \tag{6}$$

Eq. (6) is the volume-averaged charge balance equation for the lithium ions in the electrolyte in the cathode.

$$\frac{dc_1^{s,avg}}{dt} = -3\frac{j_1}{r_1} \tag{7}$$

Eq. (7) is used to calculate the average concentration of lithium in the active material in the cathode.

$$D_{s,1}\frac{c_1^{s,surf}-c_1^{s,avg}}{r_1} = -\frac{j_1}{5} \tag{8}$$

Eq. (8) is used to calculate the surface concentration of lithium on the active material particle surface in the cathode.

2.2.2. Separator equations

$$\frac{dc_2}{dt} = \frac{\frac{-2(D(c_{12},T))(c_2-c_1)}{\frac{l_1}{\varepsilon_1^{b_1}}+\frac{l_2}{\varepsilon_2^{b_2}}} + \frac{2(D(c_{23},T))(c_3-c_2)}{\frac{l_2}{\varepsilon_2^{b_2}}+\frac{l_3}{\varepsilon_3^{b_3}}}}{\varepsilon_2 l_2} \tag{12}$$

Eq. (12) is the volume averaged mass conservation equation in the separator.

2.2.3. Anode equations

The following equations are used to model the physical and electrochemical processes within the anode of the cell.

$$\frac{dc_3}{dt} = \frac{\frac{-2(D(c_{23},T))(c_3-c_2)}{\frac{l_2}{\varepsilon_2^{b_2}}+\frac{l_3}{\varepsilon_3^{b_3}}}}{\varepsilon_3 l_3} + a_3(1-t_i)\frac{j_3}{l_3} \tag{13}$$

Eq. (13) is the volume-averaged mass balance equation for the lithium ions in the electrolyte in the anode.

$$i_{app} = -2\kappa\left(c_{23},T\right)\frac{\left(\phi_{l,3}-\phi_{l,2}\right)}{\left(\frac{l_3}{\varepsilon_3^{b_3}}+\frac{l_2}{\varepsilon_2^{b_2}}\right)} + \frac{4RT(1-t_i)}{F}\frac{\kappa\left(c_{23},T\right)\left(c_{l,3}-c_{l,2}\right)}{\left(\frac{l_3}{\varepsilon_3^{b_3}}+\frac{l_2}{\varepsilon_2^{b_2}}\right)c_{23}} \tag{14}$$

Eq. (14) is the volume-averaged charge balance equation for the lithium ions in the electrolyte in the anode.

$$\frac{dc_3^{s,avg}}{dt} = -3\frac{j_3}{r_3} \tag{15}$$

Eq. (15) is used to calculate the average concentration of lithium in the active material in the anode.

$$D_{s,3}\frac{c_3^{s,surf}-c_3^{s,avg}}{r_3} = -\frac{j_3}{5} \tag{16}$$

Eq. (16) is used to calculate the surface concentration of lithium on the active material particle surface in the anode.

$$\frac{-i_{app}}{Fa_3l_3} = k_3(c_3)^{\alpha_{a,3}}\left(c_3^{s,max}-c_3^{s,surf}\right)^{\alpha_{a,3}}\left(c_3^{s,surf}\right)^{\alpha_{c,3}}\left(exp\left(\frac{\alpha_{a,3}F\eta_3}{RT}\right)-exp\left(\frac{-\alpha_{c,3}F\eta_3}{RT}\right)\right) \tag{17}$$

$$\frac{i_{app}}{Fa_1l_1} = k_1(c_1)^{\alpha_{c,1}}\left(c_1^{s,max}-c_1^{s,surf}\right)^{\alpha_{a,1}}\left(c_1^{s,surf}\right)^{\alpha_{c,1}}\left(exp\left(\frac{\alpha_{a,1}F\eta_1}{RT}\right)-exp\left(\frac{-\alpha_{c,1}F\eta_1}{RT}\right)\right) \tag{9}$$

Eq. (9) is the Butler-Volmer equation for the intercalation reaction at the cathode.

Surface overpotential (η_1) in Eq. (9) is given by the calculation performed in Eq. (10),

$$\eta_1 = \phi_{s,1}-\phi_{l,1}-U\left(c_1^{s,surf}\right) \tag{10}$$

Eq. (11) is for calculating concentration of lithium ions at the cathode-separator interface:

$$c_{12} = \left(\frac{\frac{\varepsilon_1^{b_1}}{l_1}c_1+\frac{\varepsilon_2^{b_2}}{l_2}c_2}{\frac{\varepsilon_1^{b_1}}{l_1}+\frac{\varepsilon_2^{b_2}}{l_2}}\right) \tag{11}$$

Eq. (17) is the Butler-Volmer equation for the intercalation reaction at the anode.

Surface overpotential (η_3) in Eq. (17) is given by the calculation performed in Eq. (18),

$$\eta_3 = \phi_{s,3}-\phi_{l,3}-U\left(c_3^{s,surf}\right) \tag{18}$$

Eq. (19) is for calculating concentration of lithium ions at the anode-separator interface:

$$c_{23} = \left(\frac{\frac{\varepsilon_3^{b_3}}{l_3}c_3+\frac{\varepsilon_2^{b_2}}{l_2}c_2}{\frac{\varepsilon_3^{b_3}}{l_3}+\frac{\varepsilon_2^{b_2}}{l_2}}\right) \tag{19}$$

2.2.4. Heat generation equations

The following equations are used to calculate the individual heat generation elements used in Eq. (3) above. For these equations, the subscripts $i = 1$ corresponds to cathode, $i = 2$ corresponds to separator, and $i = 3$ corresponds to anode.

$$q_{irrev,i} = \frac{i_{app}}{l_i}\eta_i, \quad i \in (1,3) \tag{20}$$

Eq. (20) is used for the calculation of the irreversible heat generation within the cathode and anode of a cell.

$$q_{rev,i} = \frac{i_{app}}{l_i} T_i \left[\frac{\partial U\left(c_i^{s,surf}\right)}{\partial T} \right], i \in (1,3) \tag{21}$$

Eq. (21) is used to calculate the reversible heat generation within the cathode, and anode of the battery cell.

$$q_{ohm,1} = \frac{\left| i_{app}\left(\phi_{l,12} - \phi_{l,1}\right) \right|}{l_1}; \quad q_{ohm,2} = \frac{\left| i_{app}\left(\phi_{l,12} - \phi_{l,23}\right) \right|}{l_2}; \quad q_{ohm,3} = \frac{\left| i_{app}\left(\phi_{l,23} - \phi_{l,3}\right) \right|}{l_3} \tag{22}$$

The equations within Eq. (22) are the calculations performed for the ohmic heat generation of the cathode, separator, and anode.

The individual anode, cathode, and separator heat generations are added up for each source of heat generation: irreversible, reversible, and ohmic heat generation. Thus, one term is used for each source: q_{irrev}, q_{rev}, and q_{ohm}.

$$q''' = q_{irrev} + q_{rev} + q_{ohm} \tag{23}$$

The total volumetric heat generation of the battery cell given by Eq. (23) will be used in the volume-averaged thermal model in Eq. (4).

Additional constitutive relations required for coupled electrochemical-thermal simulations are provided in Appendix A.

2.2.5. Additional information

Detailed analysis of the Tank-in-Series model and comparison to other models, including the standard experimentally validated P2D model, can be found in the paper by Subramaniam et al. [45,69]. This model demonstrates excellent agreement with the computationally intensive P2D model by M. Doyle et al. [42], while capable of performing a charge or discharge simulation in the range of a few milliseconds, a fraction of the time taken by the P2D model to simulate the same.

By combining physics-based modeling of individual cells in a battery pack and capturing spatial and temporal variation of temperature in the battery pack, a greater understanding of the underlying temperature-dependent electrochemical processes in batteries across the battery pack can be achieved, providing a pathway to gain deeper insights into the pack-level cell balancing, degradation, and safety issues. The process of linking the volume-averaged pack-level thermal model with the cell-level electrochemical model, and in turn linking the individual cells in series and parallel connections to form a battery pack, is provided next.

2.3. Electrical model

To simulate a battery pack consisting of a number of cells, a 0D electrical model to implement series-parallel electrical connections is coupled with the electrochemical model. In this work, parallel branches are considered to be separate modules within the pack design. Each module consists of a number of cells connected in series. The pack configuration is considered to be like the one shown in the schematic in Fig. 1. Eq. (24) given below is used to implement parallel connection between modules by matching the voltage across modules. The resistance of the connector is ignored but can be incorporated by modifying Eq. (24). Eq. (25) imposes the summation of the currents associated with each cell/module to a specified value based on the pack-level current. In Eq. (24), V_{pos} is the positive terminal voltage of a module, with the numbering in the subscript indicating the module number. It should be noted that the positive terminal voltage of a module corresponds to the positive electrode potential of the first cell in that module. The negative terminal of each module is set as the reference potential which is

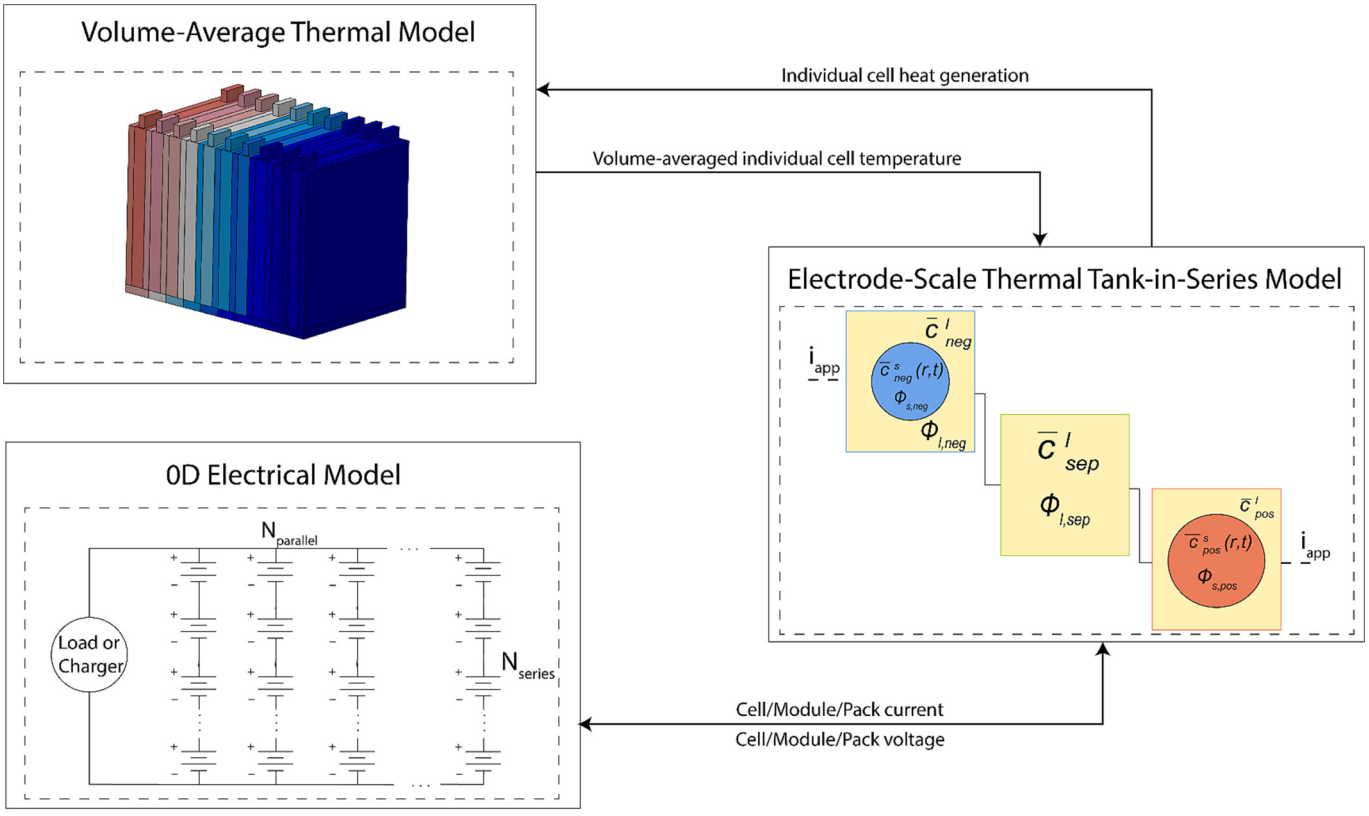

Fig. 1. Schematic detailing coupling among electrochemical-thermal-electrical models, shown as blocks for graphical representation. The cell and coolant channel arrangement shown in Fig. 1 for the Volume-Averaged Thermal Model block are representative of a BTMS using a cold plate with fins.

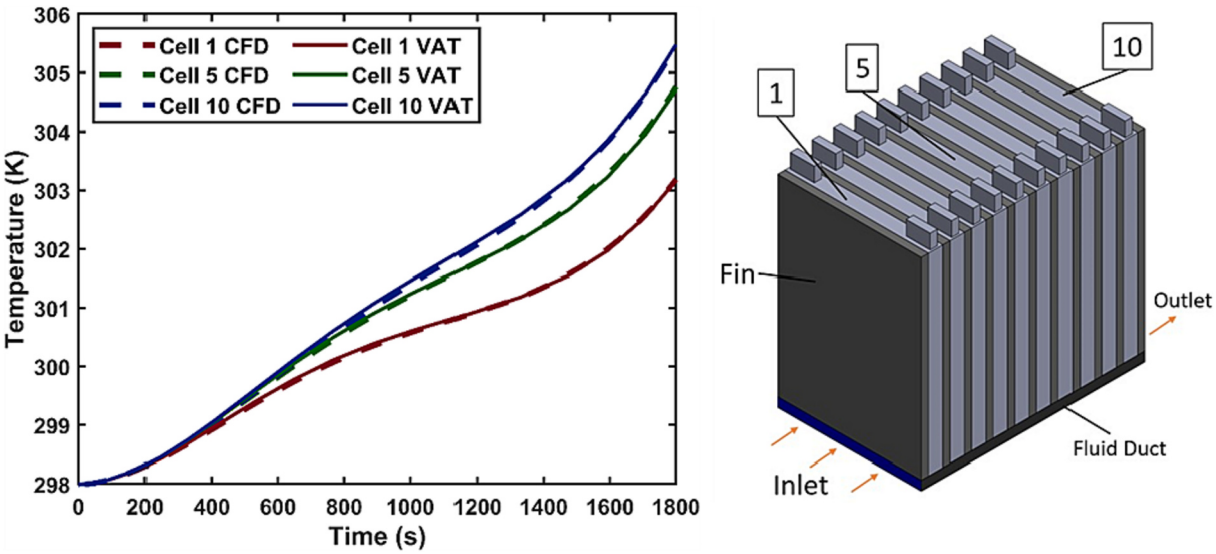

Fig. 2. (a) Volume-averaged and full-order thermal model comparison for a prismatic cell pack section, (b) Schematic of a prismatic cell pack section.

discussed in further detail while discussing series connection between cells in a module. Similarly, in Eq. (25), I_y is the current in a module, with y representing the module number. Here, I_{app} is the overall current applied to or withdrawn from the battery pack. This I_{app} is related to the applied current density, i_{app}, in the electrochemical model through the cross section area of the electrode.

$$V_{pos,1} = V_{pos,2} = V_{pos,3} = \ldots V_{pos,n} \tag{24}$$

$$\sum I_y = I_{app} \tag{25}$$

For modeling series connections between cells in a module, the negative terminal potential (solid-phase anode potential) of each cell is equated to the positive terminal potential (solid phase cathode potential) of the next cell in the series connection. The voltage drop due to the resistance offered by the electrical connector is accounted here. For the last cell in the series connection in each module, the negative terminal potential (solid phase anode potential) is set as the reference potential for convenience. The reference potential can be placed at a different location such that the voltage drop in the connections from cell negative terminal to the load/charger negative terminal can be accounted in the model calculations. In addition to this coupling, due to the nature of series connections, the current passing through each cell in series within a module is the same. In Eq. (26), x represents the numbering of cells connected in a particular module, and y represents the numbering of the modules, similar to the subscripts in Eq. (24) and Eq. (25). The additional subscript used in Eq. (26) differentiates between the anode and cathode cell terminals.

$$V_{x+1,y,cathode} + \left|I_y{}^{*}R_{connector}\right| = V_{x,y,anode} \tag{26}$$

2.4. Framework coupling

The overall simulation framework with the coupling of various models is depicted in Fig. 1. The volume-averaged thermal model is informed by heat generation values calculated by the Tank-in-Series model, and in turn, the Tank-in-Series electrochemical model is informed by the volume-averaged cell temperature values calculated from the volume-averaged thermal model. Additionally, the Tank-in-Series model and the 0D electrical model exchange voltage and current information to model series and parallel cell and module connections in the battery pack. By coupling these models together in this manner, a versatile, computationally fast, and efficient simulation approach is proposed to study battery pack performance under a variety of operating conditions for different pack configurations and thermal management designs, as well as predict internal state variables of individual battery cells in a pack. The coupled equations are solved in MATLAB using ode15s, a solver for differential algebraic equations (DAEs) in MATLAB.

The volume-averaged thermal models are developed using the approach outlined in subsection 2.1 for two battery pack configurations, one with prismatic/pouch cells stacked in modules with coolant channels running parallel along the length of the modules (Fig. 2 (b)) and the other with cylindrical cells and coolant channel similar to the Tesla Model S EV battery pack (Fig. 3 (b)). For the simplification of calculations, assumptions are made for the heat transfer within the BTMS. For these calculations, the thermal energy is assumed to flow into the much lower thermal resistance pathway offered by the coolant in coolant channels than the surrounding air. Thus, heat transfer into the air in the gaps between the cells and surrounding the cells is ignored. Additionally, for the pack configuration shown in Fig. 3 (b), conduction heat transfer between cells is ignored. These assumptions/limitations are only present in the validation cases and not in the subsequent simulation cases. A constant average convective heat transfer coefficient, h, is considered on the surface of each cell while accounting for the change in convective heat transfer coefficient across cells, especially in the regions where the coolant flow is thermally developing. As discussed earlier, the convective heat transfer coefficients used in the volume-averaged thermal models are calculated from steady-state CFD simulations performed using COMSOL Multiphysics.

3. Results and discussions

The results from the proposed volume-averaged thermal (VAT) model are compared against the full-order CFD simulation performed using COMSOL Multiphysics. The volumetric heat generation data used in these simulations are obtained from the literature [70,71]. Fig. 2 (a) shows a comparison between the two for a representative section of a prismatic/pouch battery cell pack using the dynamic heat generation rate corresponding to a 1C discharge. Fig. 3 (a) shows the same comparison for a representative section of a cylindrical battery cell pack using the dynamic heat generation rate corresponding to a 2C discharge.

For the validation shown in Figs. 2 (a) and 3 (a), the effect of developing flow on heat transfer is captured by considering the change in convective heat transfer coefficient in the entry region. The change in h in this region is shown in Fig. 1 of the supplementary material. In subsequent simulation studies (Fig. 5 to Fig. 9), the entry effect of

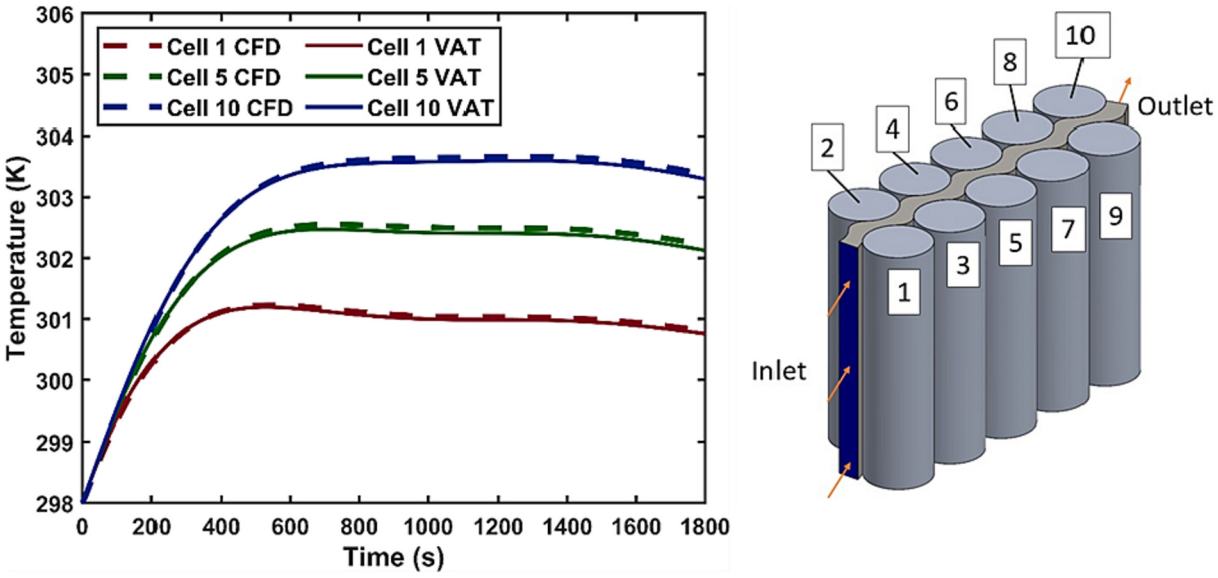

Fig. 3. (a) Volume-averaged and full-order thermal model comparison for a cylindrical cell pack section, (b) Schematic of a cylindrical cell pack section.

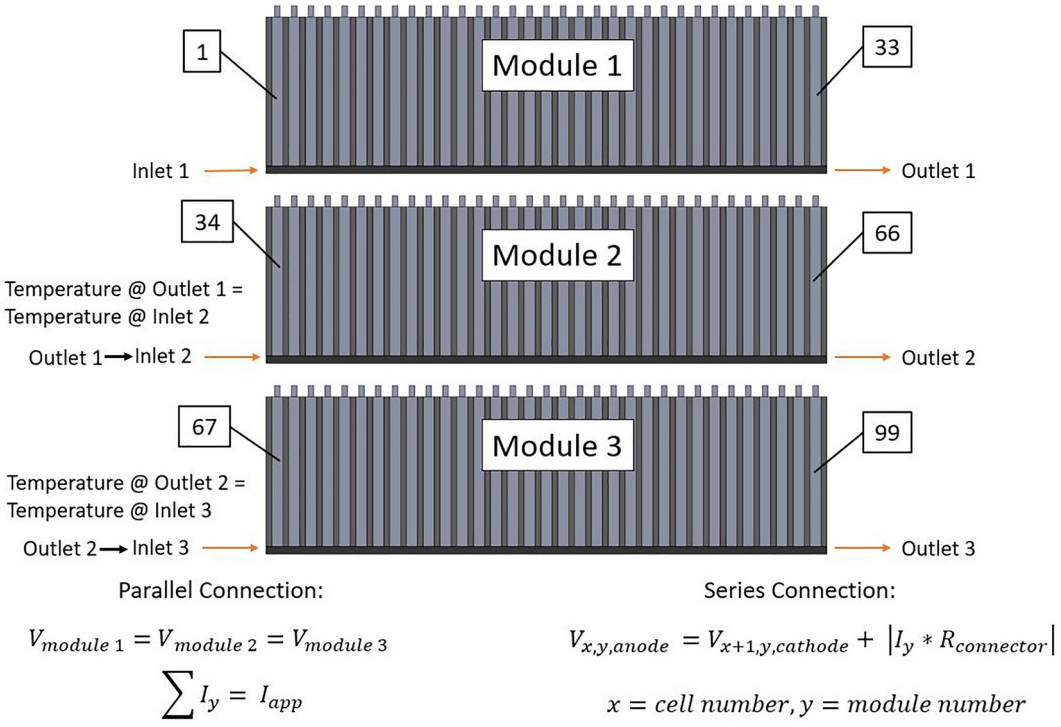

Fig. 4. Schematic for the battery pack simulated in the rest of results and discussion section.

coolant flow is ignored for simplicity, and the convective heat transfer coefficient is considered constant and set to 50 W/(m^{2}K). Figs. 2 (a) and 3 (a) present the COMSOL Multiphysics simulation results, represented by the dashed lines, and the volume-averaged thermal model simulation results, represented by the solid lines. The average temperatures obtained from the volume-averaged thermal model simulations are in excellent agreement with COMSOL Multiphysics. As shown in Figs. 2 (a) and 3 (a), the proposed volume-averaged thermal modeling approach is validated for both a prismatic/pouch type battery pack section and a cylindrical battery cell pack section. This shows the versatility of the volume-averaging approach for modeling heat transfer in battery packs.

In all subsequent simulation studies, the proposed volume-averaged thermal model will be coupled with multiple sets of Tank-in-Series electrochemical model equations, where each set represents each cell in the pack. Additionally, a battery module is considered to be composed of multiple cells connected in series, and multiple such modules are connected in parallel, forming the battery pack in all the coupled simulations. This type of arrangement is chosen for demonstration purposes only, and any series-parallel arrangement of cells and modules can be modeled using the proposed approach by modifying the equations to

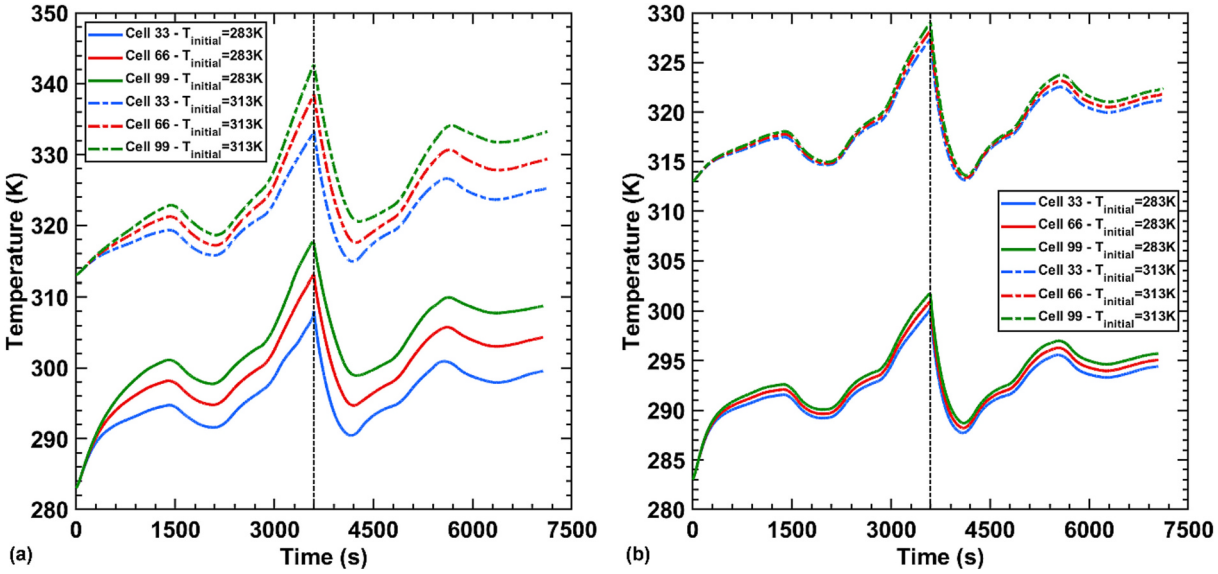

Fig. 5. Cell temperature plotted against time for the last cell in each module in two different scenarios, a high initial/inlet temperature of 313 K and a low initial/inlet temperature of 283 K (a) Plot showing the two temperature conditions with a low coolant mass flow rate (b) Plot showing the two temperature conditions with a high coolant mass flow rate.

model electrical connections discussed in subsection 2.3 appropriately. Each module consists of 33 cells in series. There are 3 such modules connected in parallel in the pack. As depicted in Fig. 4, cells are numbered 1 through 99 beginning at the coolant inlet such that cells 1–33 are in the first module, 34–66 are in the second, and 67–99 are in the last, with cell 99 adjacent to the coolant outlet. The coolant is considered to be flowing sequentially such that coolant leaving one module enters the next module, as shown in Fig. 4. This pack configuration is chosen for demonstration purposes only, and the proposed approach can be applied to any given coolant flow configuration by making appropriate changes to the volume-averaged thermal equations in their discretized form. This same pack configuration is used in other figures and analyses unless specified otherwise. In each scenario, the inlet temperature of the coolant and the initial temperature of the pack are taken to be the same as the outside surrounding temperature. In other words, the inlet temperature of the coolant is not considered to be controlled and assumed to be at the same temperature as the surrounding temperature. Information on the type of battery cell used and its dimensions can be found in Table 5. In the first study, the battery pack is discharged down to the pack voltage of 99 V at 1C and then charged up to 138.6 V. This corresponds to the desired discharge and charge terminal voltage of 3.0 and 4.2 V, respectively, for each cell.

The temperature of the last cell in each module of the battery pack as a function of time is plotted in Fig. 5 for two different cases: one where the initial pack temperature is set to 283 K and the other with the initial pack temperature considered to be 313 K. These cases will be referred to as the 283 K case and the 313 K case in subsequent discussions. These temperature values are chosen to simulate two extreme case temperature scenarios. In Fig. 5 (a), the mass flow rate (MFR) for the coolant is chosen such that a significant temperature variation (>5 K) occurs

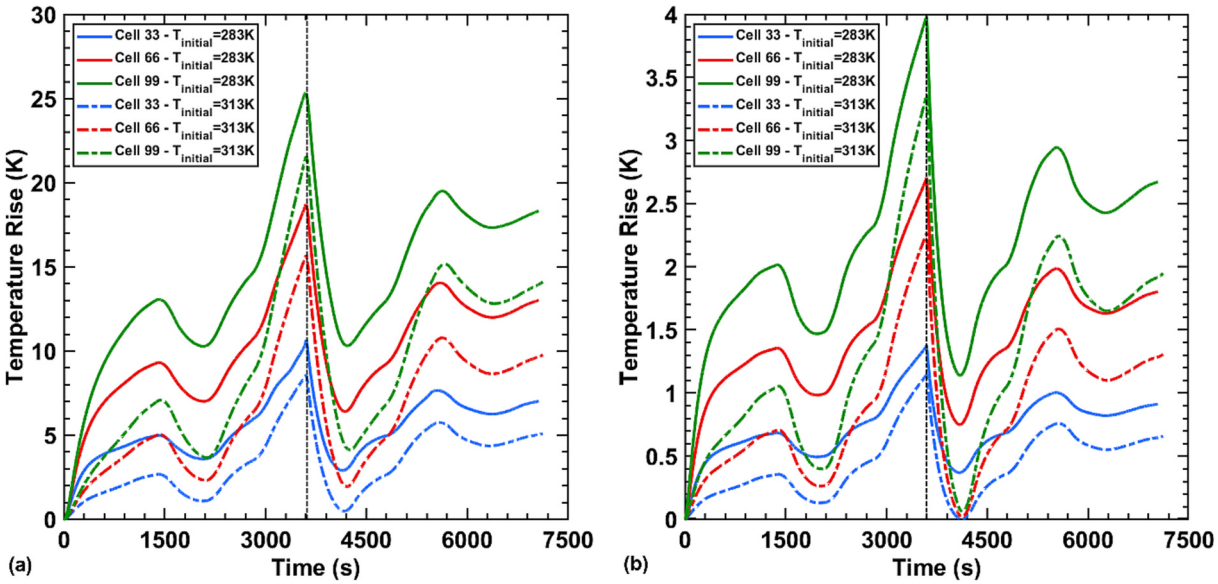

Fig. 6. Coolant temperature rise plotted against time for the last cell in each module in two different scenarios, a high initial/inlet temperature of 313 K and a low initial/inlet temperature of 283 K (a) Plot showing the two temperature conditions with a low coolant mass flow rate, (b) Plot showing the two temperature conditions with a high coolant mass flow rate.

across the cells in the pack. Fig. 5 (b) considers a relatively high mass flow rate for the coolant, resulting in a more uniform temperature across the modules and the pack (<2 K temperature variation across the pack).

Both figures show that the cell temperature follows a similar temporal evolution in all the scenarios, with the cell heating up during the discharge cycle due to ohmic heat, irreversible reaction heat, and largely exothermic entropic heat of the reactions and reaching the maximum cell temperature of the full discharge-charge cycle at the end of discharge. This is followed by the cell cooling down due to the endothermic entropic heat of reactions strongly influencing overall heat generation as charging begins. In the later stage of charging, the temperature rises again due to a net positive entropic heat combined with irreversible reaction heat and ohmic heat. The difference in the mass flow rate leads to the differences in cell temperatures as well as the maximum temperature in the pack which will be observed at cell 99 in the pack configuration considered. In Fig. 5 (a), the temperature of cell 99 increases by approximately 35 K and 30 K for the 283 K and 313 K cases, respectively, while in Fig. 5 (b), the same cell under the same two temperature conditions experiences a temperature rise 19 K and 16 K, respectively. An interesting item of note is that although the higher mass flow rate led to a decrease in the maximum cell temperature in the pack by a factor of almost 2, the variation in temperature across the pack dropped significantly more (<2 K for high MFR vs 10 K for low MFR), by a factor of over 6.

In Fig. 5, as discussed above, the cell temperature is plotted against time for the last cell in each module for 4 different scenarios. For the same scenarios, the rise in coolant temperature from the inlet temperature has been plotted in Fig. 6 for the volume of coolant adjacent to each of these cells, with Fig. 6 (a) showing a low mass flow rate scenario and Fig. 6 (b) showing a high mass flow rate scenario. The temperature trends seen in Fig. 6 are almost identical to those in Fig. 5, albeit with a temperature increase smaller in magnitude than those seen in Fig. 5, due to the effect of convective thermal resistance. In the case of Fig. 6 (a), the coolant temperature rise is significant (maximum coolant temperature rise >20 K near cell 99) due to the coolant moving slower and having more time to absorb heat from the cells compared to the high mass flow rate scenario considered in Fig. 6 (b) with much smaller coolant temperature rise (maximum coolant temperature rise<5 K near cell 99). It should be noted that the coolant temperature rise is noticeably higher for the 283 K case than the 313 K case (approximately 25 K for the 283 K case vs. 21 K for the 313 K case for low mass flow rate), particularly for the low mass flow rate case. This is because of the increased irreversible reaction heat due to lower reaction rate constant and increased ohmic heat because of the sluggish electrolyte transport at low temperatures.

For results shown in Fig. 7, three battery packs, each with a different series-parallel configuration, are simulated through a discharge-charge cycle at 1C for the 283 K case. The three configurations considered for this figure are: (1) 9 modules connected in parallel with 11 cells connected in series in each, (2) 3 modules connected in parallel with 33 cells connected in series in each, and (3) 1 module with 99 cells connected in series.

In Fig. 7 (a), the cell voltages for 3 cells in each configuration have been plotted against time, while Fig. 7 (b) shows the current for each module in each configuration over time. Fig. 7 (c) shows the relationship between the current distribution between modules and temperature variation across the battery pack by varying coolant mass flow rates. In Fig. 7 (a), the first cells in the first, middle, and last module of the 11s9p configuration are chosen as the representative cells. The cells in the same position (i.e., cell #) are chosen for the other 2 configurations so that location-based temperature differences do not influence the voltage results presented. The convention for current in these simulations, and all others in this study, is to use a negative current for discharge and a positive current for charging. The cutoff voltages for charge and discharge are chosen to be 33 V (11s9p), 99 V (33s9p), 297 V (99s1p) and 46.2 V(11s9p), 138.6 V (33s3p), 415.8 V (99s1p) for discharge and charge, respectively. In each configuration, the cutoff voltages are chosen such that they correspond to an average cell voltage of 3.0 V for discharge and 4.2 V for charge.

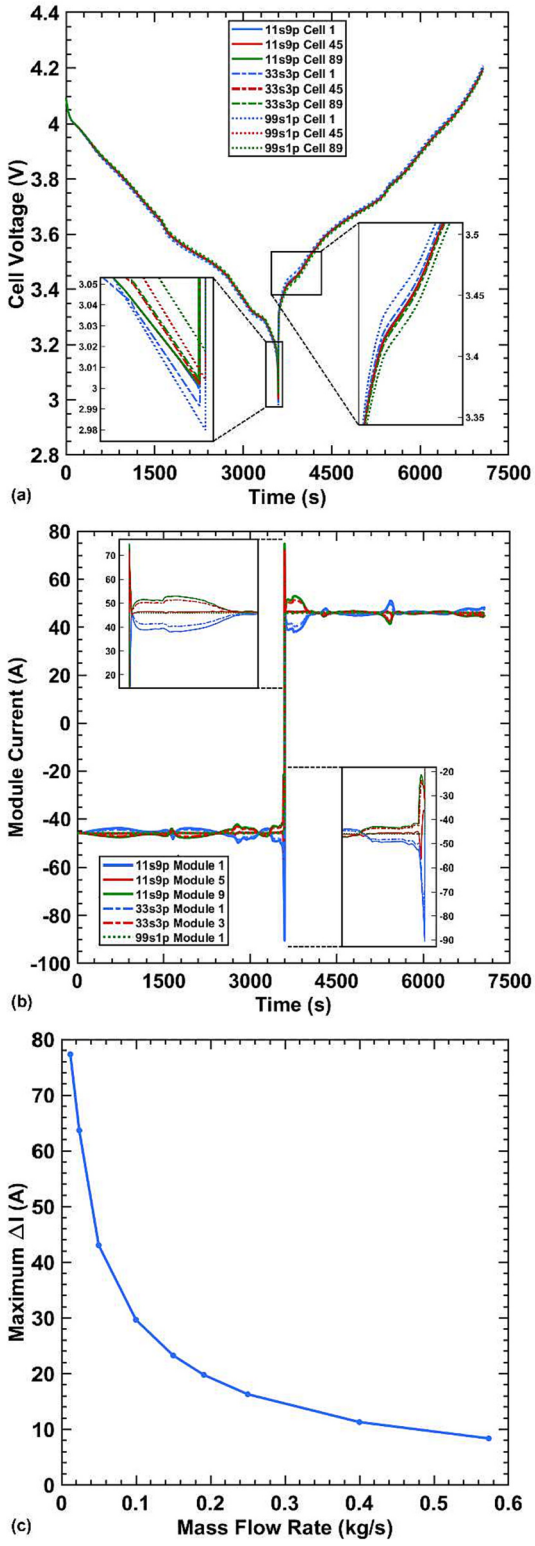

Fig. 7. (a) Cell voltage plotted against time for the same 3 cells in three different pack configurations, (b) Current through each module plotted against time for 3 different pack configurations, (c) The maximum difference in current draw among modules, maximum ΔI, plotted against coolant mass flow rate.

In the voltage plot shown in Fig. 7 (a), the voltage curves for the three chosen cells are nearly identical across all three pack configurations, and the minute variations are insignificant to the cell performance (charge

and discharge capacity and energy delivered or stored) when only one cycle is considered. It should be noted that the voltage difference increases to its maximum near the end of discharge (40 mV for 11s9p configuration - see zoomed-in portion at the end of discharge). This effect propagates, and a voltage difference of approximately the same magnitude can be seen near the first hump at the beginning of charge (see zoomed-in portion after start of charge). The cell voltage curves at the same hump feature during the discharge portion of the plot have been found to show almost no variation (relatively). This suggests that these small differences in voltages may compound over time, leading to potential and charge imbalances across cells within the pack and promoting increasingly uneven aging.

In Fig. 7 (b), for the pack configurations with modules connected in parallel (11s9p and 33s3p), the current is distributed mostly evenly across modules for almost the entire discharge and charge processes, except towards the end of the discharge and the early stage of charge. For example, at the end of the discharge, there is a noticeable difference in current distribution across modules, with the first module providing the highest current and the last module providing the lowest current (see zoomed-in portion at the end of discharge). This difference tends to increase with increase in the number of parallel branches (referred to as modules in this study), as visible in Fig. 7 (b), where the 11s9p configuration shows the highest variation in the current between Module 1 and Module 9. Since the total pack current must remain unchanged, higher current being drawn from certain modules (e.g., Module 1 in 11s9p at the end of discharge) is countered by lower current being drawn from the other modules (e.g., Module 9 in 11s9p at the end of discharge). This behavior is the result of cells in modules at relatively lower temperatures experiencing sluggish transport in the electrolyte as well as slower reaction kinetics. This causes the cells in modules at lower overall temperatures to have slightly less lithiated cathode active material than the cells in modules at higher overall temperatures. Towards the end of discharge, this leads the cells in modules at higher overall temperatures to experience a sharp increase in the charge transfer resistance to the reduction reaction at the cathode as the lithium concentration in the cathode of these cells approaches the maximum concentration ahead of the cells in modules at lower temperatures. Since the same voltage is imposed across modules connected in parallel, the current being withdrawn from the module with cells experiencing higher charge transfer resistance goes down. Since the total amount of current drawn from the pack remains unchanged, the drop in current associated with some modules must be compensated by an equal overall increase in current from the other modules. During the early stage of charging, the opposite current distribution is observed as the cells in modules at lower overall temperatures draw less current due to their higher overall resistance because of the sluggish electrolyte transport and slower charge transfer kinetics. To confirm that the uneven current distribution is indeed due to temperature variation across the pack, we repeated the above simulation at different mass flow rates. As the increase in mass flow rate would lead to more uniform temperatures across the pack, the uneven current distribution at the end of discharge would reduce. Similarly, a reduction in mass flow rate would lead to an increase in uneven current distribution. This exact trend is shown in Fig. 7 (c), where the maximum difference in the current being drawn from modules at a time near the end of discharge is plotted against mass flow. This result supports the hypothesis proposed to explain the uneven current distribution among modules in the pack. A key item to note is that this brief but important uneven current distribution induced by temperature difference does not lead to a noticeable change in cell voltage across the modules (see Fig. 7 (a)). Hence, only monitoring cell voltage may not help detect this type of behavior, which may result in cell balancing and uneven degradation issues if repeated over multiple cycles.

It is well known that slight manufacturing variation in the battery cell can cause enough variations in the design parameters, such as electrode thickness, active material particle radius, and porosity, and that it may lead to a noticeable change in charge and discharge behavior across cells [72]. The effect of these variations on the individual cells in a battery pack, as well as on the aggregate pack-level characteristics, is relatively less understood. To study this, a 0.2% variation is applied to each cell's electrode thicknesses, porosities, and particle radii in a randomized manner. In Fig. 8 (a), the cell voltage of 3 cells has been plotted along with a fourth baseline curve where the cells had no manufacturing variation. Cells 28 and 29 are chosen because their end-of-discharge voltages are the farthest below and above the desired 3 V cutoff, respectively. It should be noted that a pack-level cutoff voltage of 99 V and 138.6 V is applied for discharge and charge, respectively, for both the simulations. In Fig. 8 (b), the temperature of all the cells within the battery pack has been plotted at 4 different times, both with and without considering the manufacturing variation. The four times chosen include halfway through the discharge cycle, the end of the discharge cycle,

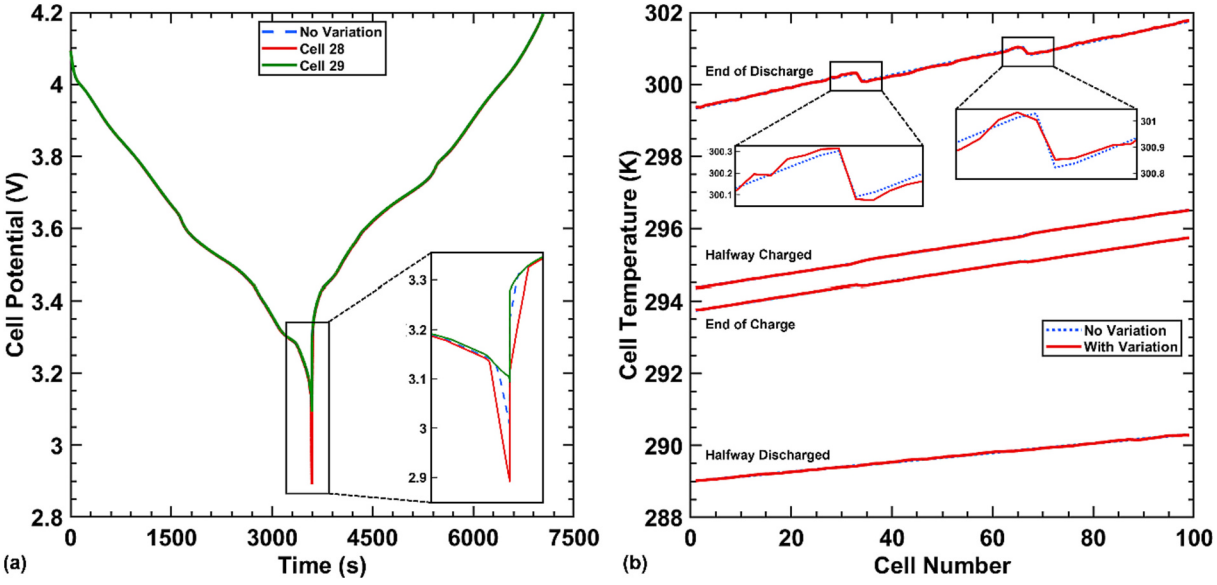

Fig. 8. (a) Cell voltage plotted against time for three cells that were lowest, average, and highest voltage at the end of discharge along with a baseline curve from a cell with no simulated manufacturing variation, (b) Cell temperature plotted against cell number both with and without simulated manufacturing variation in electrode thickness, porosity, and particle radii at four different times – halfway through discharge, end of discharge, halfway through charge, and end of discharge.

halfway through the charge cycle, and lastly, the end of the charge cycle.

As shown in Fig. 8 (a), when manufacturing variation is considered, the voltage curves of the selected cells across the pack appear to be identical, matching with the baseline case without variation at almost all times during the discharge and charge process. However, near the end of the discharge, significant variation in cell voltages can be observed across cells in the presence of manufacturing variation as well as clear deviation from the case without variation (baseline). For example, cell 29 was only discharged to about 3.1 V, while Cell 28 was discharged close to 2.9 V. This difference is around 0.2 V, which is significant, especially considering that this has occurred over just one discharge with all cells being at the same voltage and SOC at the beginning of discharge. In the absence of variation, all cells are observed to discharge very close to 3.0 V. Interestingly, the cells return to roughly the same voltage at the end of the charge. This can be attributed to the fact that, in the simulated scenario, the anode particles do not become fully lithiated during charging, whereas the cathode particles get fully lithiated during discharge. Hence, the small variation in surface concentration, electrolyte concentration, and reaction kinetics does not cause substantial voltage variation at the end of charge, like it does at the end of discharge. Since the variation in cell voltage across the pack demonstrates a somewhat random behavior and does not seem to be related to the cell location within the pack or module, which would have indicated the effect of temperature variation across the pack and module being the driving force for this behavior, it can be attributed to the randomized manufacturing variation considered in this simulation study. This voltage variation across cells in the pack at the end of discharge and beginning of charge can initiate uneven degradation, causing further potential and charge imbalances among cells and modules, which will be studied in a subsequent study.

As expected, the temperature curves in Fig. 8 (b) show that the cell temperature increases monotonically with cell number at each time, except for the time corresponding to the end of the discharge. The curve corresponding to the end of discharge time shows an unexpected module-to-module temperature change. While the temperature increases with cell number within a module as expected due to coolant heating up as it flows past Cell 1 to Cell 99, a small yet noticeable decrease in temperature from the last cell in one module to the first cell in the next module can be observed. This can be explained by the uneven currents across modules seen in Fig. 7 (b). The uneven current distribution across these modules will directly affect the entropic, ohmic, and polarization heat generation rate in the cells across modules. The module operating at a lower overall temperature throughout the discharge (e.g., Module 1) experiences the highest current towards the end of discharge, which causes its heat generation rate to be higher than the next module (e.g., Module 2) at the end of discharge. Module 2 experiences less heat generation during this time period due to the relatively small current being drawn from it, resulting in cells in Module 2 experiencing smaller temperature rise towards the end of discharge compared to cells in Module 1. In this particular case, the smaller temperature rise experienced by the cells in Module 2 is enough to result in the last cell of Module 1 reaching a higher temperature than the first cell of Module 2 at the end of discharge, as shown in Fig. 8 (b). This exact same explanation can also be applied to understand the temperature drop going from the last cell of Module 2 to the first cell of Module 3. The temperature trends at other times largely show expected linear, monotonically increasing cell temperature across the pack. This finding showcases the complexity of the relationships between electrochemical, thermal, and heat transfer phenomena at the pack-level, and the usefulness of the modeling framework developed in this work to improve understanding of these complex relationships. Additionally, this type of change in cell-to-cell temperature at such locations can be detected by strategically placed thermocouples. This can help detect the underlying electrochemical behavior, in this case, the uneven current distribution among modules in a battery pack. The behavior discussed above is observed in both the cases, the one with manufacturing variation and the one without (baseline). Unlike cell voltage, consideration of manufacturing variation based on the parameters chosen in this study has little and inconsequential effect on the cell temperature across the pack, as shown by the dashed line in Fig. 8 (b).

Fig. 9 plots the battery pack voltage as a function of time for a discharge and charge cycle. In Fig. 9 (a), two MFRs are considered to study the effect of mass flow rate and resulting temperature variation in the pack on the pack voltage. In Fig. 9 (b), the effect of manufacturing variation discussed earlier is compared with the baseline case in terms of the pack-level voltage. Again, the same two extreme temperature scenarios as before are considered in both figures. Discharge and charge rates of 1C are chosen for this study.

Fig. 9 (a) shows the effect of initial/inlet temperatures and temperature variation across the pack on the pack voltage due to the temperature-dependent properties such as transport, thermodynamics, and kinetic properties. The same two mass flow rates, as considered in

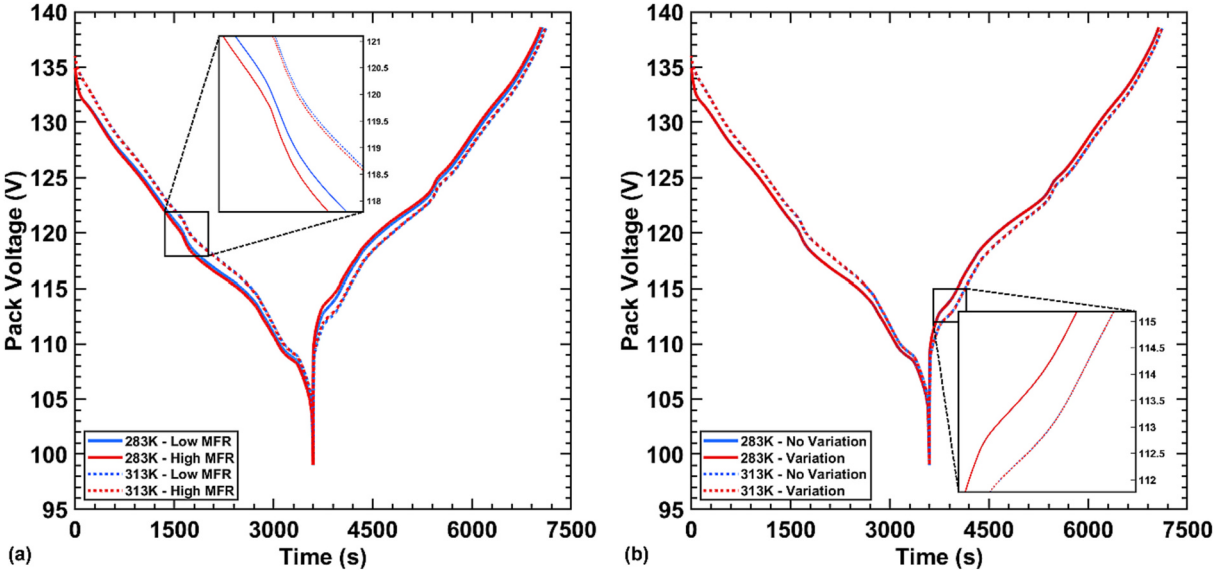

Fig. 9. Pack voltage plotted against time for two initial/inlet temperatures, 283 K and 313 K with: (a) a high and low coolant mass flow rate with a cutout showing the distribution of voltage curves, (b) simulated manufacturing variation and baseline curves with no simulated manufacturing variation at each temperature.

Fig. 6 (a) and (b), are used to produce two cases with high (≈10 K) and low (<2 K) temperature variations across the pack. There is a noticeable difference in the voltage curves for the 283 K case and the 313 K case, with the 283 K showing more energy loss due to overall lower voltage through the discharge and higher voltage through the charge. This is consistent with the high temperature rise in the coolant for the 283 K case, as shown in Fig. 6 (a), suggesting greater loss of energy due to higher heat generation compared to the 313 K case. It can also be observed that mass flow rate makes a more noticeable effect on pack-level voltage for the 283 K case compared to the 313 K case. Interestingly, low mass flow rates (high temperature variation) lead to lower energy losses compared to the high mass flow rate case (low temperature case). This can be explained by the fact that the use of a high mass flow rate for the 283 K case leads to the pack operating at an overall lower temperature than the low mass flow rate case. This leads to more heat generation losses in the high mass flow rate case compared to the low mass flow rate case, particularly for the 283 K case, where almost all cells will operate under suboptimal thermal conditions from the efficiency perspective. The additional energy loss in operating the pump to achieve the specified mass flow is not considered. Finally, it should be noted that the effect of mass flow rate on the uneven current distribution among modules does not influence the pack-level voltage, and hence, pack-level voltage is not useful in detecting the same.

Fig. 9 (b) shows the effect of manufacturing variation under the same extreme temperature scenarios as before. Unlike Fig. 8 (a), which shows variation in individual cell voltages across the pack due to manufacturing variation, pack-level voltage fails to show any such effect. This suggests that the effect of the randomly assigned variation in cell parameters to capture cell manufacturing variation within the cells in the pack averages out and becomes unnoticeable in the pack-level voltage and capacity predicted by the model, at least over one discharge-charge cycle. This is an important finding as it clearly shows, as expected, the failure of pack/module level voltage in giving any indication of cell-level voltage variations due to cell-to-cell manufacturing variations. The variations at the cell level, as discussed previously, may compound over time to create a meaningful difference in these pack-level performance variables over the lifetime of the pack, which will be the focus of a future study.

To further demonstrate the capability and usefulness of the proposed modeling framework, a scenario with rapidly changing temperatures due to a rapid decline in coolant inlet temperature is simulated. This scenario represents a possible failure scenario where the thermal management system is unable to maintain the inlet temperature of the coolant, and the coolant temperature undergoes rapid cooling due to the low ambient temperature of 278 K. In Fig. 10 (a), cell temperature is plotted for select cells across the battery pack. Initially, the cell temperature increases rapidly due to the low initial temperature of the cell, causing substantial heat generation during the early stage of the discharge and the coolant entering the battery pack at 308 K. The cell temperature continues to vary dynamically throughout the discharge, primarily in response to the dynamically varying entropic heat at both cathode and anode. At the beginning of the charge process, as shown in Fig. 4 (a), the cell temperature drops first due to the substantial net negative entropic heat generation and subsequently increases due to overall heat generation rising as charging progresses. Near the end of charge process, the coolant temperature is rapidly dropped to 278 K to simulate thermal management failure scenario, which results in temperature of the cells dropping rapidly as well, with Cell 1 experiencing the temperature drop the first and the largest due to its proximity to the inlet. In Fig. 10 (b), cell voltages of the same cells are plotted against time from the same simulation. All cell voltages appear to be identical throughout the discharge and charge processes, except at the very end of the charge process. The rapid drop in the cell temperatures shown in Fig. 10 (a) leads to sluggish electrolyte transport in the cells. In the case of Cell 1, this causes the electrolyte concentration to become very small, causing a rapid increase in the voltage at the very end of charge process, with the Cell 1 voltage going as high as 4.4 V followed by a slight drop due to the drop in current to the module with Cell 1. This type of overcharging of certain cells may go undetected as only pack and module voltages are typically monitored by the BMS. This may pose a safety issue as well as cause/promote uneven degradation in the pack and the module.

All the simulation results from the electrochemical-thermal modeling framework presented in Fig. 5–10 are summarized in Table 3 below.

Although the general approach of developing volume-averaged thermal-fluid models can be applied to virtually any thermal management design, the volume-averaged equations provided in the present paper are specific to single-phase systems with laminar fluid flow. The heat transfer by radiation between cells, as well as the cell and pack enclosure, are not explicitly considered in the present volume-averaged heat transfer calculations. Heat transfer between cells via the busbar

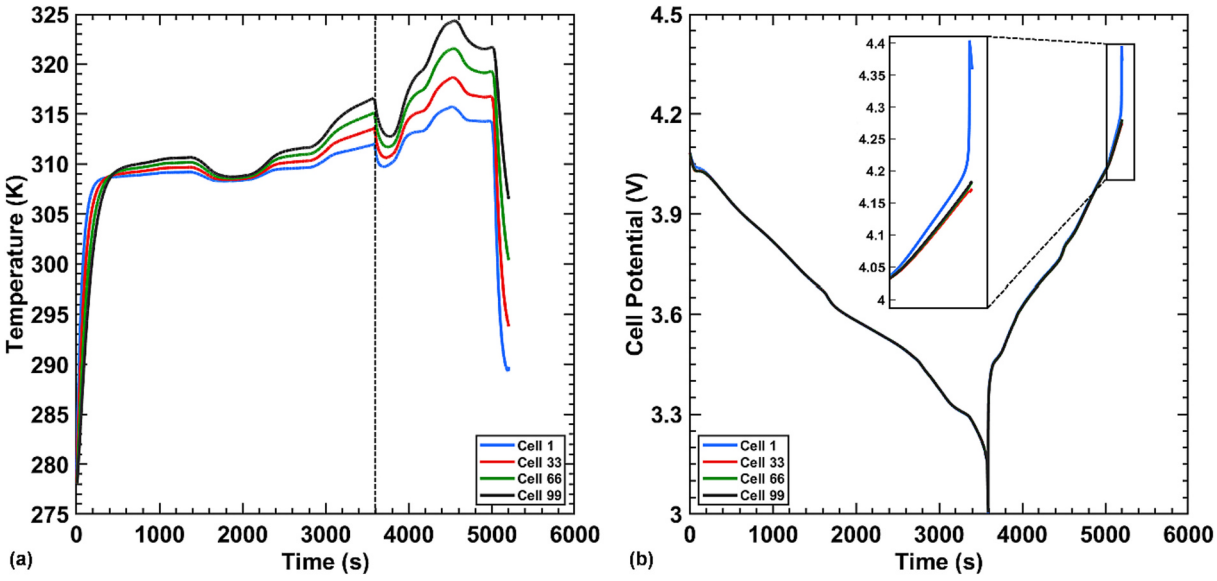

Fig. 10. For a scenario with rapid change in coolant inlet temperature, (a) a plot of cell temperature against time for 4 different cells, (b) a plot of cell potential against time for the same 4 cells.

Table 3
Table showing the main parameters for each simulation used in each figure as well as the key findings from each figure.

Figure	Configuration	C-rate	Inlet temperature	Initial and ambient temperature	Mass flow rate	Key findings
5a	33s3p	1C	283 K,313 K	283 K,313 K	Low	High mass flow rate reduces the cell temperature rise in the pack to almost half and the temperature variation across the pack by a factor of 6 compared to low mass flow rate. Low ambient temperature leads to greater cell and coolant temperature rise as well as temperature variation across pack.
5b	33s3p	1C	283 K,313 K	283 K,313 K	High	
6a	33s3p	1C	283 K,313 K	283 K,313 K	Low	
6b	33s3p	1C	283 K,313 K	283 K,313 K	High	
7a	33s3p, 50s2p, 99s1p	1C	298 K	298 K	Low	Current variation within a pack, which can cause charge imbalance and uneven aging, is inversely proportional to mass flow rate in a nonlinear manner and worsens with more modules/cells in parallel.
7b	33s3p, 50s2p, 99s1p	1C	298 K	298 K	Low	
8a	33s3p	1C	283 K,313 K	283 K,313 K	High	A maximum cell voltage variation of over 0.2 V is observed at the end of discharge in the presence of simulated manufacturing variation in the pack.
8b	33s3p	1C	283 K,313 K	283 K,313 K	High	
9a	33s3p	1C	283 K,313 K	283 K,313 K	Low, High	While manufacturing variation and cell temperature variation have negligible effect, cell operating temperature has a noticeable effect of over 1 V at times on the pack voltage.
9b	33s3p	1C	283 K,313 K	283 K,313 K	Low	
10a	33s3p	1C	Varying	278 K	High	Rapidly changing cell temperature due to a sudden drop in the coolant temperature led to an overcharge of 0.2 V for one cell before the specified pack cut-off voltage is reached.
10b	33s3p	1C	Varying	278 K	High	

connecting cells is not accounted for either. These additional complexities and heat transfer mechanisms can be incorporated into the proposed general framework by introducing additional volume-averaged heat equations for the relevant domain, modifying existing volume-averaged equations for the coolant and cell, and using appropriate boundary conditions to capture heat transfer between different heat-exchanging bodies in the pack. In electrochemical modeling, spatial temperature variation within a cell is ignored, and volume-averaged cell temperature is used instead. This is a reasonable approach, except at very high C-rates ($\geq$3C) and in the case of large-format cells [73]. It should also be noted that the electrochemical model used in this framework is a volume-averaged version of the well-known P2D model, and therefore, it is not valid at a very high C-rate ($\geq$5C). It is worth pointing out that the alternative to the volume-averaged modeling approach would involve a full-order CFD simulation coupled with electrochemical model for individual cells, which, as mentioned previously, would have drastically higher computational demand and simulation time due to the orders of magnitude difference in the number of equations that need to be solved for the two approaches. A detailed comparative analysis of the two approaches in terms of accuracy, versatility, simulation time, and computational demand would be helpful in determining the most suitable approach for a given specific set of conditions and battery pack design.

The capability of the proposed modeling framework can be expanded in the future by the research community by incorporating aging/degradation models in this framework. This can enable the study of pack-level capacity and power loss while analyzing the uneven degradation that may be taking place at the individual cell-level. This would enable the analysis of different pack configurations/architectures and composition, battery cell type (form factor, chemistry, etc.), and thermal management system design in the context of performance, life, and safety of the battery pack. Additionally, this pack-level model can be used to perform stochastic analysis by taking into account the effect of cell-to-cell manufacturing variation and other sources of uncertainty in battery pack aging and failure. Finally, this framework can be coupled with vehicle dynamics for EVs and flight dynamics models for electric aircraft to simulate battery packs under real-world operating conditions for these applications, whether in a simulation study to guide design of battery system or as a live virtual twin of the battery for use by the battery management system. This capability can further help design and optimize battery packs tailored to these applications.

4. Conclusion

This study presents an innovative and versatile approach that integrates a volume-averaged heat transfer model with the Tank-in-Series electrochemical model, enabling a comprehensive analysis of large battery systems, including the ability to provide fundamental insights into pack level performance and safety issues. This modeling framework can be tailored to accommodate various thermal management designs and battery pack configurations, allowing for fast yet detailed electrochemical-thermal simulations of large battery packs. Our findings underscore the significance of factors like coolant mass flow rate, operating temperature, and manufacturing variations in shaping the thermal and electrochemical behavior of battery packs. First, we have quantified the influence of temperature variations within a battery pack on current distribution among parallel-connected modules, revealing potential fundamental causes behind charge imbalance in battery module/pack. Notably, increasing coolant mass flow rate, and thereby reducing temperature variation within a module/pack, may help mitigate this issue. Secondly, the study has meticulously examined the repercussions of cell-to-cell manufacturing variations on voltage disparities within the battery pack. Such disparities can result in cell over-discharging, raising concerns about accelerated degradation and safety. Importantly, our pack-level results indicate that the presence of these complex phenomena may not be noticeable in the typical pack/module voltage monitored by the Battery Management Systems (BMS). Additionally, the impact of rapidly changing inlet temperatures on cell behavior has been investigated and cells experiencing extreme thermal conditions exhibited significant variations in their electrochemical behavior, such as one cell overcharging while others staying below the cutoff voltage. Finally, the modeling framework proposed in this study can be integrated with aging models to explore uneven degradation, cell balancing issues, accelerated performance loss, and safety implications in battery packs.

CRediT authorship contribution statement

S. Jordan: Writing – review & editing, Writing – original draft, Visualization, Methodology, Investigation, Formal analysis. **O. Schreiber:** Writing – review & editing, Writing – original draft, Visualization, Validation, Methodology. **M. Parhizi:** Writing – review & editing, Methodology. **K. Shah:** Writing – review & editing, Writing – original draft, Supervision, Project administration, Methodology, Investigation, Formal analysis, Conceptualization.

Declaration of competing interest

The authors declare the following financial interests/personal relationships which may be considered as potential competing interests:

Krishna Shah reports financial support and equipment, drugs, or supplies were provided by Alabama Transportation Institute. Krishna Shah reports financial support and travel were provided by Center for Advanced Vehicle Technologies, Alabama Transportation Institute. Owen Schreiber reports financial support was provided by The University of Alabama Graduate School.

Data availability

Data will be made available on request.

Acknowledgement

The authors would like to acknowledge valuable contributions of Dr. Suryanarayana Kolluri by providing the initial code for the Tank-in-series battery model and overall guidance. K. Shah would like to acknowledge graduate student and travel support from the Alabama Transportation Institute (ATI) and the Center for Advanced Vehicle Technologies (CAVT), respectively, at the University of Alabama. This work has been presented at the 242nd meeting of the Electrochemical Society in Atlanta, Georgia and NASA Aerospace Battery Workshop 2022 in Huntsville, Alabama. O. Schreiber would like to acknowledge the Graduate School at the University of Alabama for supporting him through the award of National Alumni Association Fellowship in the AY 2022-23.

Appendix A. Appendix

Table 4
Constitutive relations used in the electrochemical and thermal model.

Constitutive relations used in the electrochemical and thermal model
$D(c_i,T) = 0.0001\times 10^{-\left[4.43+\frac{54}{T-229-0.005c_i}\right]-0.00022c_i}, i\in\{1,2,3\}$
$\kappa(c_i,T) = 1\times 10^{-4}c_i\left[\begin{array}{c}(-10.5+0.0740T-6.96\times 10^{-5}T^2)\\ +c_i(0.668-0.0178T+2.8\times 10^{-5}T^2)\\ +c_i^2(0.494-8.86\times 10^{-4}T^2)\end{array}\right]^2, i\in\{1,2,3\}$
$U_i(T,\theta_i) = U_{i,ref}(T_{ref},\theta_i)+(T-T_{ref})\left[\frac{dU_i}{dT}\right]\Big\vert_{T_{ref}}, i\in\{1,3\}$
$D^s_{i,eff} = D^s_i exp\left(-\frac{E_a^{D^s_i}}{R}\left[\frac{1}{T}-\frac{1}{T_{ref}}\right]\right), i\in\{1,3\}$
$a_i = \frac{3}{R_i}(1-\varepsilon_i-\varepsilon_{f,i}), i\in\{1,2,3\}$
$(1-t_+^0)\left(1+\frac{\partial lnf}{\partial lnc_i}\right) = 0.601-7.5894\times 10^{-3}c_i^{0.5}+3.1053\times 10^{-5}(2.5236-0.0052T)c_i^{1.5},\ i\in\{1,2,3\}$
U_p, U_n, $\frac{dU_p}{dT}$, and $\frac{dU_n}{dT}$ are obtained by extracting data from Sturm et al. [74]

Table 5
Additional equations solved in electrochemical model.

Additional constitutive equations for the Tank-in-Series model
$j_1 = k_1 {c_1}^{\alpha_{a,1}}\left(c_1^{s,max,1}-c_1^{s,surf}\right)^{\alpha_{a,1}}\left(c_1^{s,surf}\right)^{\alpha_{c,1}}\left(exp\left(\frac{\alpha_{a,1}F\eta_1}{RT_1}\right)-exp\left(\frac{-\alpha_{c,1}F\eta_1}{RT_1}\right)\right) = \frac{i_{app}}{a_1 l_1 F}$
$j_3 = k_3 {c_3}^{\alpha_{a,3}}\left(c_3^{s,max,3}-c_3^{s,surf}\right)^{\alpha_{a,3}}\left(c_3^{s,surf}\right)^{\alpha_{c,3}}\left(exp\left(\frac{\alpha_{a,3}F\eta_3}{RT_i}\right)-exp\left(\frac{-\alpha_{c,3}F\eta_3}{RT_i}\right)\right) = -\frac{i_{app}}{a_3 l_3 F}$
$\phi_{l,12} = \left(\frac{\frac{\varepsilon_1^{b_1}}{l_1}\phi_{l,1}+\frac{\varepsilon_2^{b_2}}{l_2}\phi_{l,2}}{\frac{\varepsilon_1^{b_1}}{l_1}+\frac{\varepsilon_2^{b_2}}{l_2}}\right)$
$\phi_{l,23} = \left(\frac{\frac{\varepsilon_3^{b_3}}{l_3}\phi_{l,3}+\frac{\varepsilon_2^{b_2}}{l_2}\phi_{l,2}}{\frac{\varepsilon_3^{b_3}}{l_3}+\frac{\varepsilon_2^{b_2}}{l_2}}\right)$

Table 6
Configuration a (prismatic cell BTMS) simulation properties.

Prismatic/pouch cell battery pack configuration		
Density	1917	kg m^{-3}
Specific Heat	940	J kg^{-1} K^{-1}
Thermal Conductivity	1.03	W m^{-1} K^{-1}
Cell Width	150	Mm
Cell Thickness	15	Mm
Cell Height	200	Mm
Channel Dimensions		
Channel Height	10	Mm
Channel Width	150	Mm
Coolant Fluid	Water	

Table 7
Configuration b (cylindrical cell BTMS) simulation properties.

Cylindrical cell battery pack configuration		
Density	2719	kg m^{-3}
Specific Heat	1300	J kg^{-1} K^{-1}
Thermal Conductivity	3.4	W m^{-1} K^{-1}
Cell Diameter	18	mm
Cell Height	65	Mm
Channel Dimensions		
Channel Height	65	Mm
Channel Thickness	5.96	Mm
Coolant Fluid	Water	

Appendix B. Supplementary data

Supplementary data to this article can be found online at https://doi.org/10.1016/j.apenergy.2024.122746.

References

[1] Summary E. National blueprint for lithium batteries 2021-2030. D.o. Energy; 2021.
[2] Jaguemont J, et al. Lithium-ion battery aging experiments at subzero temperatures and model development for capacity fade estimation. IEEE Trans Veh Technol 2015;65(6):4328–43.
[3] Lin X, et al. Lithium plating mechanism, detection, and mitigation in lithium-ion batteries. Prog Energy Combust Sci 2021;87:100953.
[4] Peng X, et al. A review of the estimation and heating methods for lithium-ion batteries pack at the cold environment. Energy Sci Eng 2019;7(3):645–62.
[5] Zilberman I, et al. Online aging determination in lithium-ion battery module with forced temperature gradient. J Energ Storage 2020;28:101170.
[6] Waldmann T, et al. Temperature dependent ageing mechanisms in Lithium-ion batteries–a post-mortem study. J Power Sources 2014;262:129–35.
[7] Han X, et al. A review on the key issues of the lithium ion battery degradation among the whole life cycle. ETransportation 2019;1:100005.
[8] Chiu K-C, et al. Cycle life analysis of series connected lithium-ion batteries with temperature difference. J Power Sources 2014;263:75–84.
[9] Feng X, et al. Mechanisms for the evolution of cell variations within a LiNixCoyMnzO2/graphite lithium-ion battery pack caused by temperature non-uniformity. J Clean Prod 2018;205:447–62.
[10] Omariba ZB, Zhang L, Sun D. Review of battery cell balancing methodologies for optimizing battery pack performance in electric vehicles. IEEE Access 2019;7:129335–52.
[11] Docimo DJ, Fathy HK. Analysis and control of charge and temperature imbalance within a lithium-ion battery pack. IEEE Trans Control Syst Technol 2018;27(4):1622–35.
[12] Rao Z, Wang S. A review of power battery thermal energy management. Renew Sust Energ Rev 2011;15(9):4554–71.
[13] Yang N, et al. Unbalanced discharging and aging due to temperature differences among the cells in a lithium-ion battery pack with parallel combination. J Power Sources 2016;306:733–41.
[14] Rahn CD, Wang C-Y. Battery systems engineering. John Wiley & Sons; 2013.
[15] Saw LH, Ye Y, Tay AA. Integration issues of lithium-ion battery into electric vehicles battery pack. J Clean Prod 2016;113:1032–45.
[16] Offer GJ, et al. Module design and fault diagnosis in electric vehicle batteries. J Power Sources 2012;206:383–92.
[17] Juarez-Robles D, et al. Overdischarge and aging analytics of Li-ion cells. J Electrochem Soc 2020;167(9):090558.
[18] Zhang G, et al. Comprehensive investigation of a slight overcharge on degradation and thermal runaway behavior of lithium-ion batteries. ACS Appl Mater Interfaces 2021;13(29):35054–68.
[19] Zhu X, et al. Overcharge investigation of large format lithium-ion pouch cells with Li (Ni0. 6Co0. 2Mn0. 2) O2 cathode for electric vehicles: Thermal runaway features and safety management method. Energy 2019;169:868–80.
[20] Rothgang S, Baumhofer T, Sauer DU. Diversion of aging of battery cells in automotive systems. In: 2014 IEEE vehicle power and propulsion conference (VPPC). IEEE; 2014.
[21] Song Z, et al. A study of cell-to-cell variation of capacity in parallel-connected lithium-ion battery cells. ETransportation 2021;7:100091.
[22] Schuster SF, et al. Lithium-ion cell-to-cell variation during battery electric vehicle operation. J Power Sources 2015;297:242–51.
[23] Rumpf K, Naumann M, Jossen A. Experimental investigation of parametric cell-to-cell variation and correlation based on 1100 commercial lithium-ion cells. J Energ Storage 2017;14:224–43.
[24] Liu X, et al. The effect of cell-to-cell variations and thermal gradients on the performance and degradation of lithium-ion battery packs. Appl Energy 2019;248:489–99.
[25] Baumhöfer T, et al. Production caused variation in capacity aging trend and correlation to initial cell performance. J Power Sources 2014;247:332–8.
[26] Preger Y, et al. Degradation of commercial lithium-ion cells as a function of chemistry and cycling conditions. J Electrochem Soc 2020;167(12):120532.
[27] Chen Y, et al. A review of lithium-ion battery safety concerns: the issues, strategies, and testing standards. J Energ Chem 2021;59:83–99.
[28] Feng X, et al. Thermal runaway mechanism of lithium ion battery for electric vehicles: a review. Energ Storage Mater 2018;10:246–67.
[29] Zhang J, et al. An overview on thermal safety issues of lithium-ion batteries for electric vehicle application. IEEE Access 2018;6:23848–63.
[30] Doughty DH, Roth EP. A general discussion of Li ion battery safety. Electrochem Soc Interf 2012;21(2):37.
[31] Duh Y-S, et al. Characterization on thermal runaway of commercial 18650 lithium-ion batteries used in electric vehicles: a review. J Energ Storage 2021;41:102888.
[32] Waldmann T, et al. Post-mortem analysis of aged lithium-ion batteries: disassembly methodology and physico-chemical analysis techniques. J Electrochem Soc 2016;163(10):A2149.
[33] Kuntz P, et al. Identification of degradation mechanisms by post-mortem analysis for high power and high energy commercial li-ion cells after electric vehicle aging. Batteries 2021;7(3):48.
[34] Hu X, Li S, Peng H. A comparative study of equivalent circuit models for Li-ion batteries. J Power Sources 2012;198:359–67.

[35] Nejad S, Gladwin D, Stone D. A systematic review of lumped-parameter equivalent circuit models for real-time estimation of lithium-ion battery states. J Power Sources 2016;316:183–96.
[36] Akbarzadeh M, et al. A comparative study between air cooling and liquid cooling thermal management systems for a high-energy lithium-ion battery module. Appl Therm Eng 2021;198:117503.
[37] Liu Z, et al. Shortcut computation for the thermal management of a large air-cooled battery pack. Appl Therm Eng 2014;66(1–2):445–52.
[38] Xu X, Tong G, Li R. Numerical study and optimizing on cold plate splitter for lithium battery thermal management system. Appl Therm Eng 2020;167:114787.
[39] Cao W, et al. Thermal modeling of full-size-scale cylindrical battery pack cooled by channeled liquid flow. Int J Heat Mass Transf 2019;138:1178–87.
[40] Chung Y, Kim MS. Thermal analysis and pack level design of battery thermal management system with liquid cooling for electric vehicles. Energy Convers Manag 2019;196:105–16.
[41] Tete PR, Gupta MM, Joshi SS. Numerical investigation on thermal characteristics of a liquid-cooled lithium-ion battery pack with cylindrical cell casings and a square duct. J Energ Storage 2022;48:104041.
[42] Doyle M, Fuller TF, Newman J. Modeling of galvanostatic charge and discharge of the lithium/polymer/insertion cell. J Electrochem Soc 1993;140(6):1526.
[43] Guo M, Sikha G, White RE. Single-particle model for a lithium-ion cell: thermal behavior. J Electrochem Soc 2010;158(2):A122.
[44] Tanim TR, Rahn CD, Wang C-Y. A temperature dependent, single particle, lithium ion cell model including electrolyte diffusion. J Dyn Syst Meas Control 2015;137 (1).
[45] Subramaniam A, et al. Properly lumped Lithium-ion battery models: a tanks-in-series approach. J Electrochem Soc 2019;167(1):013534.
[46] Safari M, et al. Multimodal physics-based aging model for life prediction of Li-ion batteries. J Electrochem Soc 2008;156(3):A145.
[47] Yang X-G, et al. Modeling of lithium plating induced aging of lithium-ion batteries: transition from linear to nonlinear aging. J Power Sources 2017;360:28–40.
[48] Ai W, Wu B, Martínez-Pañeda E. A coupled phase field formulation for modelling fatigue cracking in lithium-ion battery electrode particles. J Power Sources 2022; 544:231805.
[49] Schimpe M, et al. Comprehensive modeling of temperature-dependent degradation mechanisms in lithium iron phosphate batteries. J Electrochem Soc 2018;165(2): A181.
[50] Yang S-C, et al. A coupled electrochemical-thermal-mechanical degradation modelling approach for lifetime assessment of lithium-ion batteries. Electrochim Acta 2019;326:134928.
[51] Kupper C, Bessler WG. Multi-scale thermo-electrochemical modeling of performance and aging of a LiFePO4/graphite lithium-ion cell. J Electrochem Soc 2016;164(2):A304.
[52] Reniers JM, Mulder G, Howey DA. Review and performance comparison of mechanical-chemical degradation models for lithium-ion batteries. J Electrochem Soc 2019;166(14):A3189–200.
[53] Guo M, White RE. Thermal model for Lithium ion battery pack with mixed parallel and series configuration. J Electrochem Soc 2011;158(10):A1166–76.
[54] Smith K, Wang C-Y. Power and thermal characterization of a lithium-ion battery pack for hybrid-electric vehicles. J Power Sources 2006;160(1):662–73.
[55] Huang HH, et al. Thermal-electrochemical coupled simulations for cell-to-cell imbalances in lithium-iron-phosphate based battery packs. Appl Therm Eng 2017; 123:584–91.
[56] Schindler M, et al. On the impact of internal cross-linking and connection properties on the current distribution in Lithium-ion battery modules. J Electrochem Soc 2020;167(12).
[57] Wang B, et al. Study of non-uniform temperature and discharging distribution for lithium ion battery modules in series and parallel connection. Appl Therm Eng 2020;168.
[58] Basu S, et al. Coupled electrochemical thermal modelling of a novel Li-ion battery pack thermal management system. Appl Energy 2016;181:1–13.
[59] Bahiraei F, Fartaj A, Nazri G-A. Electrochemical-thermal modeling to evaluate active thermal management of a lithium-ion battery module. Electrochim Acta 2017;254:59–71.
[60] Liang J, et al. Thermal–Electrochemical simulation of electrochemical characteristics and temperature difference for a battery module under two-stage fast charging. J Energ Storage 2020;29:101307.
[61] Wang J, et al. Effect analysis on thermal behavior enhancement of lithium–ion battery pack with different cooling structures. J Energ Storage 2020;32:101800.
[62] Zadeh PG, et al. Electrochemical modeling of a thermal management system for cylindrical lithium-ion battery pack considering battery capacity fade. Case Stud Therm Eng 2022;32:101878.
[63] Pordanjani AH, et al. Thermo-electrochemical simulation of the cooling process in a compact battery pack considering various configurations. J Power Sources 2023; 553:232112.
[64] Guo Z, et al. Battery thermal management system with heat pipe considering battery aging effect. Energy 2023;263:126116.
[65] Subramaniam A, et al. An efficient electrochemical-thermal tanks-in-series model for Lithium-ion batteries. J Electrochem Soc 2020;167(11).
[66] Kuipers M, Hust F, Sauer Simon, Uwe Dirk. An in-depth view into the Tesla Model S module part two: module characterization and comparison to other state of the art EV battery systems. In: Battery power conference; 2017 (DE-HGF)24: Aachen (Germany).
[67] Whitaker S. The method of volume averagingvol. 13. Springer Science & Business Media; 1998.
[68] Zhou F. Development of closure for heat exchangers based on volume averaging theory. Los Angeles: University of California; 2014.
[69] Subramaniam A, Kolluri S, Santhanagopalan S, Subramanian VR. An efficient electrochemical-thermal tanks-in-series model for lithium-ion batteries. J Electrochem Soc 2020;167(11):113506.
[70] Hwang FS, et al. Modelling of heat generation in an 18650 lithium-ion battery cell under varying discharge rates. In: ASTFE digital library. Begel House Inc.; 2020.
[71] Chen K, Unsworth G, Li X. Measurements of heat generation in prismatic Li-ion batteries. J Power Sources 2014;261:28–37.
[72] Baumann M, et al. Parameter variations within Li-ion battery packs–theoretical investigations and experimental quantification. J Energ Storage 2018;18:295–307.
[73] Zhang Guangsheng, et al. J. Electrochem Soc 2014;161:A1499.
[74] Sturm J, et al. Modeling and simulation of inhomogeneities in a 18650 nickel-rich, silicon-graphite lithium-ion cell during fast charging. J Power Sources 2019;412: 204–23.